Digit. Signal Process. 150 (2024) 104531

Contents lists available at ScienceDirect

Digital Signal Processing

journal homepage: www.elsevier.com/locate/dsp

Robust adaptive beamforming via quasi-signal subspace estimation for covariance matrix reconstruction

Xiangwei Chen, Weixing Sheng *

School of Electronic and Optical Engineering, Nanjing University of Science and Technology, Nanjing, 210094, Jiangsu, China

ARTICLE INFO

Keywords:
Robust adaptive beamforming
INCM reconstruction
Quasi-signal subspace
Nonlinear regularization

ABSTRACT

In this paper, a novel narrowband interference-plus-noise covariance matrix (INCM) reconstruction method is proposed for robust adaptive beamforming (RAB). To enhance the effectiveness of the INCM reconstruction, we offer a prior selection of the dimension of a quasi-signal subspace (QSS) based on the signal subspace proximity employing two subsample covariance matrices (SSCMs). The QSS herein can provide estimations of all relevant factors of interference for the INCM. Moreover, by employing the eigenvectors of the SSCM, the noise power can be estimated precisely through a nonlinear regularization scheme. Finally, the signal-of-interest steering vector is corrected by an optimization problem exploiting the reconstructed INCM. The proposed RAB method can capitalize on the benefits of the QSS without prior knowledge of the number of sources. The results of the simulations demonstrate the effectiveness of the proposed method in terms of various mismatches.

1. Introduction

Adaptive beamforming has found widespread use in a variety of applications, such as radar, sonar, wireless communication and medical imaging [1–4]. The Standard Capon Beamformer (SCB) [5], as an optimal adaptive beamformer, can maximize the array output signal-to-interference-plus-noise ratio (SINR) when the theoretical interference-plus-noise covariance matrix (INCM) and precise signal-of-interest (SOI) steering vector (SV) is known. Unfortunately, in practical array systems, the covariance matrix error and SV uncertainty always exist, leading to a decrease in performance. More seriously, when the SOI is present in the training data, the SCB may be sensitive to even small estimation errors. To address this issue, numerous robust adaptive beamformers have been developed in the past decades, which can be classified into two primary types: sample-based RAB methods and reconstruction-based RAB methods.

The sample-based RAB, a classic scheme, modifies the covariance matrix or estimates the SV on the basis of the sample covariance matrix (SCM). This type of RAB methods mainly includes the diagonal loading (DL) [6–10], the eigensubspace projection (ESP) [11–14] and the SV estimation (SVE) [15–18]. The DL, as a landmark RAB method, adds a scaled identity matrix to the SCM to improve the robustness. By increasing the amount of white noise eigenvalues, the DL can possess the versatility of mitigating possible ill-conditioning of the SCM and reducing the SOI self-nulling. However, it is not an easy task to find an optimal loading level under a complex error environment. The ESP projects the SOI SV onto the signal subspace to obtain a more precise SV; from another perspective, it can be seen as a method to eliminate the noise perturbation caused by the SV mismatches or finite sample effects. The drawback of the ESP is the potential risk of subspace swap at low SNR, leading the projecting signal subspace to be contaminated by the noise component. The SVE estimate the SOI SV via convex or non-convex optimization theory, where the maximization of the capon power or minimization of the beamformer sensitivity is usually established as the objective function, while the constraint is basically set to prevent the estimate converging to the interference SV or their combinations. By establishing optimization problems, the updated SOI SV can be estimated flexibly; despite this, the performances of most SVE-based methods rely on the selected parameters.

The sample-based RAB methods have the advantage of improving the beamformer robustness without the need to consider the type of model errors. However, a commonality of this type of RAB is the performance limitation that requires making a trade-off between robustness and adaptivity. Especially at high SNR, it may substantially sacrifice the anti-interference capacity to remedy the robustness loss. This above-mentioned inherent defect of the sample-based RAB is mainly caused by the existing SOI component in the SCM for a non-ideal case. To overcome the intrinsic defect of the first robust scheme, the second

* Corresponding author.
E-mail address: shengwx@njust.edu.cn (W. Sheng).

https://doi.org/10.1016/j.dsp.2024.104531

Available online 25 April 2024

reconstruction-based RAB scheme is subsequently presented, aiming to reconstruct an interference-plus-noise covariance matrix isolating the SOI component totally. In [19], the INCM reconstruction strategy is first conducted by employing the Capon spectrum to integrate over an angular sector separated from the SOI region, and then the SOI SV is estimated through a quadratically constrained quadratic programming (QCQP) problem. To further enhance the performance under the linear errors, the method in [20] searches the interference SVs from the intersection of two sets by using the alternating projection algorithm, and the method in [21] adopts the maximum entropy power spectrum (MEPS) to replace the routine Capon spectrum estimator in the process of reconstruction. In addition, Ref. [22] takes the existing residual noise into account and then eliminates it in the noise power calculation, while Ref. [23] focus on improving the estimation accuracy of the interference powers. Recently, a Bayesian-based RAB method [24] has been developed to adjust the SV phase of the SOI, further enhancing resilience to DOA uncertainty of the SOI. Besides, considering the moving interference, the method in [25] adaptively estimates the angular region of the interference instead of using a fixed setting. The aforementioned approaches can perform far better than the classic sample-based RAB methods when the antenna array is well-calibrated, especially at high SNR. However, when the array perturbations exist, the performance will catch significant degradation. Considering the impact of array calibration errors, the reconstruction method in [26] adds a dimension of integral operation compared with [19], setting the annulus uncertainty for the interference SVs. However, to realize the algorithm [26], the uncertainty must be discretized by sampling several points, and the performance improvement over [19] is not remarkable. Afterwards, the reconstruction methods in [27,28] borrow the general rules in SVE to correct the interference SVs via solving optimization problems. Recently, the extra linear search in the complementary space for the estimation of interference SVs is presented in [29]. Besides the strategy of upgrading the nominal interference SVs to combat the array nonlinear errors, the method in [30] devises a power-based threshold strategy to make use of the advantage of the SCM at low SNR for the reconstruction. Apart from all this, several other reconstruction-based methods attempt to reduce the algorithm complexity of the reconstruction-based RAB scheme; among them, the computational process of INCM reconstruction [31–34] or the estimation of the SOI SV [35,36] is accelerated. Moreover, the study in [37] utilizes the conjugate gradient algorithm to iteratively compute the final reconstruction-based weight vector more efficiently.

In this paper, a new reconstruction-based method is devised to attain robustness against various model errors and further improve the beamformer performance. The basic idea of our approach is first to introduce a novel quasi-signal subspace (QSS). This subspace is constructed from partial eigenvectors of the SCM, and the dimension is estimated by adopting the proximity of the signal subspace of two subsample covariance matrices (SSCMs). Then, the QSS can be utilized for the estimation of interference DOAs through the framework of a MUSIC-like algorithm. Considering the presence of potential array imperfections, the QSS can be further employed to attain enhanced interference SVs with the projection method. Subsequently, the power of interference and noise is estimated, among which the interference power is obtained via a modified Capon power estimator with enhanced interference SVs. The noise power, meanwhile, is achieved by a re-estimated eigenvalue via a nonlinear regularization method. Finally, the SOI SV is updated by solving an optimization problem, which is to maximize the beamformer output power under the constraint that the estimate is not converging to any interference or their combination. To summarize, the main contributions of our work are as follows:

1. A new design for a QSS is proposed: We give a prior estimation of the dimension of QSS instead of the knowledge of the source number. The dimension selection for the QSS is theoretically established on the high proximity of two subsample signal subspaces and implemented by the approaching-zero judgment of subspace distance.
2. The relevant factors of interference are estimated in new manners based on the QSS: Different from many reconstruction-based methods employing the Capon spectrum for the estimation or pre-estimation of interference SVs and powers, we adopt a QSS-based subspace scheme to get more precise estimates for the relevant factors of interference.
3. A new method for the estimation of the noise power is proposed: Considering the noise spread issue for finite snapshots, we take advantage of the two SSCMs to design a nonlinear regularization method for the estimation of noise power.

The remainder of this paper is organized as follows. The signal model and background is introduced in Section 2. In Section 3, the proposed adaptive beamformer is detailed. In Section 4, the numerical simulations are performed under different scenarios, and the corresponding result analyses are present. Finally, the conclusion is drawn in Section 5.

Notations: $(\cdot)^H$ denotes the Hermitian transpose. $\|\cdot\|_2$ denotes the ℓ_2 norm of a vector, while $\|\cdot\|_F$ represents the Frobenius norm of a matrix. $\mathrm{Tr}\{\cdot\}$ denotes the trace of a matrix, i.e., the sum of the diagonal elements of the matrix. $\langle\cdot\rangle$ stands for the subspace spanning operator, that is, for a matrix $\mathbf{A}$, $\langle\mathbf{A}\rangle$ represents the subspace spanned by the column vectors of $\mathbf{A}$. Define a square matrix $\mathbf{B}$ with N order, $\mathbf{B}_{[n]}$ represents the first n columns of $\mathbf{B}$, $n \leqslant N$, i.e., $\mathbf{B}_{[n]} \triangleq \mathbf{B}(:, 1:n)$. $\mathbf{I}_m$ denotes the identity matrix with m dimension.

2. The signal model and background

Consider a uniform linear array (ULA) composed of N omnidirectional sensors receiving Q narrowband signals from a far field. The array observation data at the time instant k are modeled as

$$\mathbf{x}(k) = \mathbf{x}_{\mathrm{s}}(k) + \mathbf{x}_{\mathrm{i}}(k) + \mathbf{n}(k) \tag{1}$$

where $\mathbf{x}_{\mathrm{s}}(k) = s_0(k)\mathbf{a}_0$ and $\mathbf{x}_{\mathrm{i}}(k) = \sum_{q=1}^{Q-1} s_q(k)\mathbf{a}_q$ denote the components of the SOI and interference, respectively, $\mathbf{n}(k)$ is the additive white Gaussian noise vector with covariance $\sigma_{\mathrm{n}}^2\mathbf{I}$; $s_0(k)$ stands for the waveform of the SOI and $\mathbf{a}_0$ is the corresponding actual SV. $s_q(k)$ represents the waveform qth interference and $\mathbf{a}_q$ is the associated actual SV. Here, the sources and noise are assumed to be statistically uncorrelated with each other. The subspace spanned by the actual SVs of all signals is generally known as the signal subspace, denoted as

$$\langle\mathbf{A}\rangle = \mathrm{span}\left\{\mathbf{a}_0, \mathbf{a}_1, ..., \mathbf{a}_{Q-1}\right\} \tag{2}$$

In addition, the combination of actual interference SVs can span the interference subspace:

$$\langle\mathbf{A}_{\mathrm{I}}\rangle = \mathrm{span}\left\{\mathbf{a}_1, ..., \mathbf{a}_{Q-1}\right\} \tag{3}$$

The beamformer output at time instant k is given by

$$\mathbf{y}(k) = \mathbf{w}^H\mathbf{x}(k) \tag{4}$$

where $\mathbf{w}$ is the weight vector of the beamformer. The optimal weight vector can be obtained by maximizing the output SINR, defined as follows:

$$\mathrm{SINR} = \frac{\sigma_0^2\left|\mathbf{w}^H\mathbf{a}_0\right|^2}{\mathbf{w}^H\mathbf{R}_{\mathrm{i+n}}\mathbf{w}} \tag{5}$$

where σ_0^2 is the power of SOI, $\mathbf{R}_{\mathrm{i+n}}$ is the theoretical INCM. The maximization of (5) leads to the minimum variance distortionless response (MVDR) problem

$$\min_{\mathbf{w}} \mathbf{w}^H\mathbf{R}_{\mathrm{i+n}}\mathbf{w} \quad \text{s.t. } \mathbf{w}^H\mathbf{a}_0 = 1 \tag{6}$$

(6) can be calculated by adopting the Lagrangian multiplier method, and the solution is

$$\mathbf{w}_{\text{opt}} = \frac{\mathbf{R}_{\text{i+n}}^{-1}\mathbf{a}_0}{\mathbf{a}_0^H\mathbf{R}_{\text{i+n}}^{-1}\mathbf{a}_0} \tag{7}$$

Since the theoretical INCM $\mathbf{R}_{\text{i+n}}$ in (7) is unavailable in practice, the following SCM, an unbiased estimate of the theoretical covariance matrix $\mathbf{R} = \sigma_0^2\mathbf{a}_0\mathbf{a}_0^H + \mathbf{R}_{\text{i+n}}$, is usually employed as an alternative,

$$\hat{\mathbf{R}} = \frac{1}{K}\mathbf{X}\mathbf{X}^H \tag{8}$$

where $\mathbf{X} = [\mathbf{x}(1), ..., \mathbf{x}(K)]$ is the sample snapshots with the number K. Additionally, the actual SOI SV can be estimated as the nominal one based on the known array manifold as $\bar{\mathbf{a}}_0$. Then, the optimal weight vector in (8) can be rewritten in a realizable one as follows:

$$\mathbf{w}_{\text{S}} = \frac{\hat{\mathbf{R}}^{-1}\bar{\mathbf{a}}_0}{\bar{\mathbf{a}}_0^H\hat{\mathbf{R}}^{-1}\bar{\mathbf{a}}_0} \tag{9}$$

which is commonly referred to as the sample matrix inversion (SMI) beamformer. Since the signal component exists in the SCM $\hat{\mathbf{R}}$, the SMI beamformer is known to be quite sensitive to the SV mismatch and SCM error. To combat the problem mentioned above, the INCM reconstruction scheme is presented, aiming to reconstruct an INCM isolating the SOI component. The original reconstruction strategy is executed based on the Capon spectrum by integrating over an angular sector where the SOI is absent [19], that is

$$\hat{\mathbf{R}}_{\text{cm1}} = \int_{\bar{\Theta}} \frac{\mathbf{a}(\theta)\mathbf{a}^H(\theta)}{\mathbf{a}^H(\theta)\hat{\mathbf{R}}^{-1}\mathbf{a}(\theta)} d\theta \tag{10}$$

where $\bar{\Theta}$ is the complement sector of the SOI angular sector in the whole spatial domain, and $\mathbf{a}(\theta)$ is the nominal SV corresponding to the direction θ, which has the following form

$$\mathbf{a}(\theta) = \left[1, e^{j2\pi\frac{d}{\lambda}\sin(\theta)}, ..., e^{j2\pi\frac{d}{\lambda}(N-1)\sin(\theta)}\right]^T \tag{11}$$

where d is the element spacing, and λ is the signal wavelength; for (11), the rightmost sensor of the ULA is assumed to be the reference sensor. Since the integral operation in (10) contains the angular domain in which no interference lies, it inevitably introduces certain unwanted components in the reconstruction. In addition, the theoretical integral operation must be transformed to a realizable approximation form, e.g. the summation operation approximation or the Gauss-Legendre quadrature approximation. To this end, a more effective strategy is to estimate all interference SVs and the corresponding powers, together with the noise power [27–29]. Consequently, the reconstructed INCM is given as follows:

$$\hat{\mathbf{R}}_{\text{cm2}} = \sum_{q=1}^{Q-1} \hat{\sigma}_q^2\hat{\mathbf{a}}_q\hat{\mathbf{a}}_q^H + \hat{\sigma}_{\text{n}}^2\mathbf{I}_N \tag{12}$$

where $\hat{\sigma}_q^2$ and $\hat{\sigma}_{\text{n}}^2$ are the estimates of the qth interference power and noise power, respectively, $\hat{\mathbf{a}}_q$ is the qth interference SV. For many of the reconstruction methods based on strategy (12), a foundation to estimate or pre-estimate the relevant key factors (SVs and powers) of interference is the SCM-based Capon spatial spectrum, that is,

$$P_{\text{Capon}}(\theta) = \frac{1}{\mathbf{a}^H(\theta)\hat{\mathbf{R}}^{-1}\mathbf{a}(\theta)} \tag{13}$$

There are two drawbacks to the estimations on the basis of (13):
(1) Since the snapshots are limited, the spatial spectrum may contain some spurious peaks owing to the impact of noise, which leads to an overestimation of the number of interferences. An effective measure is to confirm the number of prominent spectral peaks in advance, but it also has the shortcoming that requires the knowledge of the source number for a prior.
(2) The interference powers may be underestimated if array perturbations exist.

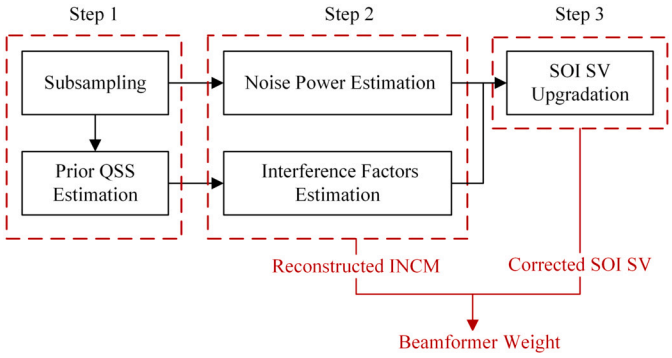

Fig. 1. Flowchart of the proposed method.

3. Proposed algorithm

In this section, a novel INCM reconstruction method for RAB is proposed. The basic idea is to reconstruct INCM via a subspace-based scheme. As depicted in Fig. 1, we first give a prior estimation of the dimension of QSS via subsampling, utilizing the proximity of two subsample signal subspaces. Afterwards, the relevant factors of interference are estimated by means of the QSS, while the noise power is estimated by a regularization method with the knowledge of subsample eigenvectors. Finally, an optimization problem of output power maximization is established to get a more precise estimate of the SOI SV.

3.1. Quasi-signal subspace estimation

3.1.1. Subsampling and signal subspace proximity under high SNR case

In the time domain, the array sample snapshots $\mathbf{X}$ can be split into two parts as $\mathbf{X} = [\mathbf{X}_1, \mathbf{X}_2]$, where $\mathbf{X}_1 \in \mathbb{C}^{N\times J}$, $\mathbf{X}_2 \in \mathbb{C}^{N\times(K-J)}$, J is the number of the first subsample. In general, since $\mathbf{X}_1$ and $\mathbf{X}_2$ are non-overlapping, the noise components of the two subsamples are considered to be independent and identically distributed. This specific property is vital for the proposed method. Subsequently, the corresponding covariance matrices of $\mathbf{X}_1$ and $\mathbf{X}_2$ can be built as $\hat{\mathbf{R}}_1 = (1/J)\mathbf{X}_1\mathbf{X}_1^H$ and $\hat{\mathbf{R}}_2 = [1/(K-J)]\mathbf{X}_2\mathbf{X}_2^H$, respectively. Performing eigendecomposition for these two SSCMs yields

$$\hat{\mathbf{R}}_1 = \mathbf{U}_1\mathbf{\Lambda}_1\mathbf{U}_1^H = \sum_{i=1}^{N} r_{1i}\mathbf{u}_{1i}\mathbf{u}_{1i}^H \tag{14}$$

$$\hat{\mathbf{R}}_2 = \mathbf{U}_2\mathbf{\Lambda}_2\mathbf{U}_2^H = \sum_{i=1}^{N} r_{2i}\mathbf{u}_{2i}\mathbf{u}_{2i}^H \tag{15}$$

where $\mathbf{\Lambda}_t$ and $\mathbf{U}_t$ denote the eigenvalue matrix and eigenvector matrix of the tth SSCM $\hat{\mathbf{R}}_t$, $t = 1, 2$, respectively, $\{r_{ti}, \mathbf{u}_{ti}\}$, $i = 1, ..., N$ are the eigenpairs of $\hat{\mathbf{R}}_t$. In general, the eigenvector matrices of $\hat{\mathbf{R}}_t$ can be portioned as

$$\mathbf{U}_t = [\mathbf{U}_{t,\text{S}}, \mathbf{U}_{t,\text{N}}],\ t = 1, 2 \tag{16}$$

where $\langle\mathbf{U}_{t,\text{S}}\rangle$ and $\langle\mathbf{U}_{t,\text{N}}\rangle$ are the corresponding signal subspace and noise subspace of $\hat{\mathbf{R}}_t$, respectively. For general notions, the dimension of $\langle\mathbf{U}_{t,\text{S}}\rangle$ is the source number Q. Here, the two subsample signal subspace $\langle\mathbf{U}_{1,\text{S}}\rangle$ and $\langle\mathbf{U}_{2,\text{S}}\rangle$ both offer asymptotically unbiased estimates of the true signal subspace, or $\langle\mathbf{A}\rangle$ in (2); for a high SNR case without subspace swap, although $\langle\mathbf{U}_{1,\text{S}}\rangle$ and $\langle\mathbf{U}_{2,\text{S}}\rangle$ are biased from the true one with high probability, the proximity between them is still high.

An important indicator to quantify the subspace proximity is the subspace distance. For two matrices $\mathbf{U}_\text{A}, \mathbf{U}_\text{B} \in \mathbb{C}^{M\times m}, m \leqslant M$ satisfying $\mathbf{U}_\text{A}^H\mathbf{U}_\text{A} = \mathbf{I}_m$, $\mathbf{U}_\text{B}^H\mathbf{U}_\text{B} = \mathbf{I}_m$, the distance between $\langle\mathbf{U}_\text{A}\rangle$ and $\langle\mathbf{U}_\text{B}\rangle$ can be define as [38,39],

$$d\left(\mathbf{U}_{\mathrm{A}},\mathbf{U}_{\mathrm{B}}\right)=2^{-1}\left\|\mathbf{U}_{\mathrm{A}}\mathbf{U}_{\mathrm{A}}^{H}-\mathbf{U}_{\mathrm{B}}\mathbf{U}_{\mathrm{B}}^{H}\right\|_{F}^{2},\\ =m-\left\|\mathbf{U}_{\mathrm{A}}^{H}\mathbf{U}_{\mathrm{B}}\right\|_{F}^{2},\ m=1,...,M \tag{17}$$

The defined distance is also named as the projection metric for a Grassmann manifold [40], and the term $\left\|\mathbf{U}_{\mathrm{A}}^{H}\mathbf{U}_{\mathrm{B}}\right\|_{F}^{2}$ is entitled as Grassmann kernel correspondingly. Observed from (17), $d\left(\mathbf{U}_{\mathrm{A}},\mathbf{U}_{\mathrm{B}}\right)\geqslant 0$. Besides, the greater the proximity of $\langle\mathbf{U}_{\mathrm{A}}\rangle$ and $\langle\mathbf{U}_{\mathrm{B}}\rangle$, the smaller $d\left(\mathbf{U}_{\mathrm{A}},\mathbf{U}_{\mathrm{B}}\right)$; especially. If $\langle\mathbf{U}_{\mathrm{A}}\rangle$ is the same with $\langle\mathbf{U}_{\mathrm{B}}\rangle$, $d\left(\mathbf{U}_{\mathrm{A}},\mathbf{U}_{\mathrm{B}}\right)=0$. According to the definition of $d\left(\mathbf{U}_{\mathrm{A}},\mathbf{U}_{\mathrm{B}}\right)$ and the proximity between $\left\langle\mathbf{U}_{1,\mathrm{S}}\right\rangle$ and $\left\langle\mathbf{U}_{2,\mathrm{S}}\right\rangle$, in such a high SNR case, we can obtain

$$d\left(\mathbf{U}_{1,\mathrm{S}},\mathbf{U}_{2,\mathrm{S}}\right)\approx 0 \tag{18}$$

To proceed, let us introduce an important property related to the subspace distance in (17) as below,

Theorem 1. *Define $\left\langle\bar{\mathbf{U}}_{\mathrm{A}}\right\rangle$ and $\left\langle\bar{\mathbf{U}}_{\mathrm{B}}\right\rangle$ as the orthogonal complement subspaces of $\langle\mathbf{U}_{\mathrm{A}}\rangle$ and $\langle\mathbf{U}_{\mathrm{B}}\rangle$, respectively. The subspace distance $d\left(\bar{\mathbf{U}}_{\mathrm{A}},\bar{\mathbf{U}}_{\mathrm{B}}\right)$ satisfies*

$$d\left(\bar{\mathbf{U}}_{\mathrm{A}},\bar{\mathbf{U}}_{\mathrm{B}}\right)=d\left(\mathbf{U}_{\mathrm{A}},\mathbf{U}_{\mathrm{B}}\right) \tag{19}$$

Proof. See Appendix A. □

According to Theorem 1, the two subsample noise subspaces $\left\langle\mathbf{U}_{1,\mathrm{N}}\right\rangle$ and $\left\langle\mathbf{U}_{2,\mathrm{N}}\right\rangle$, or in other words, the corresponding orthogonal complement subspaces of $\left\langle\mathbf{U}_{1,\mathrm{S}}\right\rangle$ and $\left\langle\mathbf{U}_{2,\mathrm{S}}\right\rangle$, also satisfy

$$d\left(\mathbf{U}_{1,\mathrm{N}},\mathbf{U}_{2,\mathrm{N}}\right)\approx 0 \tag{20}$$

3.1.2. Non-complete signal subspace proximity under relatively low SNR case

For a relatively low SNR case, the proximity described in 3.1.1 may have the potential to be not established; this is because the signal subspace swap may happen for finite snapshots, causing the signal subspace to be corrupted by the noise component. Especially when the SNR is extremely low, the subspace leakage occurs severely. Thus, the two estimated signal subspaces $\left\langle\mathbf{U}_{1,\mathrm{S}}\right\rangle$ and $\left\langle\mathbf{U}_{2,\mathrm{S}}\right\rangle$ are not pure in this case, the proximity may decrease significantly due to the independent property of noise in the time domain. On the other hand, considering the power of interference is generally strong enough compared with the weak SOI in such a low SNR case, from the perspective of the asymptotic behavior [41], we know that the probability of the $Q-1$ dominant sample eigenvalues clustering with the remaining $N-Q+1$ sample eigenvalues is very low. As a result, the subspace associated with the $Q-1$ dominant sample eigenvalues can approximate a subspace that contains the primary interference components while isolating weak components of the SOI and noise. Owing to this fact, we can ignore the corresponding Qth eigenvectors and take the first $Q-1$ eigenvectors of $\mathbf{U}_t$, $t=1,2$, that is, replace the block matrix forms in (16) with

$$\mathbf{U}_t=[\mathbf{U}'_{t,\mathrm{S}},\mathbf{U}'_{t,\mathrm{N}}],\ t=1,2 \tag{21}$$

where $\mathbf{U}'_{t,\mathrm{S}}\in\mathbb{C}^{N\times(Q-1)}$, $\mathbf{U}'_{t,\mathrm{N}}\in\mathbb{C}^{N\times(N-Q+1)}$, $\langle\mathbf{U}'_{t,\mathrm{S}}\rangle$ and $\langle\mathbf{U}'_{t,\mathrm{N}}\rangle$ are the new spanned tth non-complete signal subspace and over-complete noise subspace, respectively. In this case, the two non-complete subsample signal subspaces $\langle\mathbf{U}'_{1,\mathrm{S}}\rangle$ and $\langle\mathbf{U}'_{2,\mathrm{S}}\rangle$ mainly contains the principal components of strong interference SVs. Hence, like the two subsample signal subspaces that provide an approximation of the true signal subspace in the high SNR case, these two $Q-1$ dimension subspaces can also be treated as the subsample interference subspaces providing an approximation of the true interference subspace [42] or $\langle\mathbf{A}_{\mathrm{I}}\rangle$ defined in (3) in such a low SNR case. As a result, $\langle\mathbf{U}'_{1,\mathrm{S}}\rangle$ and $\langle\mathbf{U}'_{2,\mathrm{S}}\rangle$ possess high proximity, and similar to (18) and (20) described in 3.1.1, it can be inferred that

$$d\left(\mathbf{U}'_{1,\mathrm{S}},\mathbf{U}'_{2,\mathrm{S}}\right)\approx 0 \tag{22}$$

$$d\left(\mathbf{U}'_{1,\mathrm{N}},\mathbf{U}'_{2,\mathrm{N}}\right)\approx 0 \tag{23}$$

Notice that, for $\left\langle\mathbf{U}_{t,\mathrm{S}}\right\rangle$ or $\left\langle\mathbf{U}'_{t,\mathrm{S}}\right\rangle$, $t=1,2$, in the case of a low sample size, these sample estimators of subspaces may exhibit a relatively larger deviation from the true signal/interference subspace. Therefore, the approaching-zero property described in (20)and (23) may be weakened in this case.

3.1.3. Determination and analysis of the QSS

In this section, we intend to employ the property of high proximity discussed in 3.1.1 and 3.1.2 above to find a QSS. This QSS serves for the estimation of relevant factors of interference in the INCM reconstruction.

Suppose $\mathbf{V}_1=\mathcal{F}\left(\mathbf{U}_1\right)$, $\mathbf{V}_2=\mathcal{F}\left(\mathbf{U}_2\right)$, where $\mathcal{F}(\cdot)$ is the column flip operator, that is, the nth column of $\mathbf{V}_1$ and $\mathbf{V}_2$ satisfy $\mathbf{V}_1(:,n)=\mathbf{U}_1(:,N-n+1)$, $\mathbf{V}_2(:,n)=\mathbf{U}_2(:,N-n+1)$, respectively. Subsequently, according to the notation definition in Section 1, the first l columns of $\mathbf{V}_1$ and $\mathbf{V}_2$ can be denoted as $\mathbf{V}_{1,[l]}$ and $\mathbf{V}_{2,[l]}$, respectively. According to the expression in (17), the distance between $\left\langle\mathbf{V}_{1,[l]}\right\rangle$ and $\left\langle\mathbf{V}_{2,[l]}\right\rangle$ can be obtained as

$$d\left(\mathbf{V}_{1,[l]},\mathbf{V}_{2,[l]}\right)=l-\left\|\mathbf{V}_{1,[l]}^{H}\mathbf{V}_{2,[l]}\right\|_{F}^{2},\ l=1,...,N \tag{24}$$

For notational convenience, hereafter, we define the subspace distance in (24) as

$$d(l)=l-\left\|\mathbf{V}_{1,[l]}^{H}\mathbf{V}_{2,[l]}\right\|_{F}^{2},\ l=1,...,N \tag{25}$$

Remarks on the value of $d(l)$ are as follows:
(a) If $l<N-Q$, according to the independent property of noise in time domain mentioned in 3.1.1, the subspace proximity of $\left\langle\mathbf{V}_{1,[l]}\right\rangle$ and $\left\langle\mathbf{V}_{2,[l]}\right\rangle$ tends to be small, thus $d(l)\gg 0$ in such a case.
(b) If $l=N-Q$, $\left\langle\mathbf{V}_{1,[l]}\right\rangle$, $\left\langle\mathbf{V}_{2,[l]}\right\rangle$ are the subsample noise subspace $\left\langle\mathbf{U}_{1,\mathrm{N}}\right\rangle$, $\left\langle\mathbf{U}_{2,\mathrm{N}}\right\rangle$, respectively. Thus, it satisfies $d(l)\approx 0$ for high SNR case discussed in 3.1.1 according to (20). On the other hand, for relatively low SNR case discussed in 3.1.2, the aforementioned approaching-zero property may not be established at this point; instead, the reduction of proximity of the two subsample noise subspace may result in a certain deviation of $d(l)$ from 0; in this case, the first approaching-zero point may emerge after a delay, located at $l=N-Q+1$.

From the remarks above, letting l varies from 1 to N, we can search the first approaching-zero point of $d(l)$ in different cases. The first approaching-zero point at high SNR case should appear at $l=N-Q$, which is in accord with the dimension of the noise subspace. On the other hand, at relatively low SNR case, the first approaching-zero point may be selected as $l=N-Q+1$, which belongs to the over-complete noise subspace (or the orthogonal complement subspace of the interference subspace) as stated in 3.1.2.

To further validate the property of $d(l)$, the curves of $d(l)$ versus l under three SNR cases (SNR = 20 dB [high SNR], SNR = 0 dB [moderate-low SNR], and SNR = −20 dB [extremely low SNR]) are drawn in Fig. 2, where a 30-element ULA is considered, seven interference with interference-to-noise ratios (INRs) equal to [10, 20, 20, 30, 35, 40, 40] dB impinge on the array from different directions. It can be noted that in the high SNR case, the first approaching-zero point is located at $l=22$, i.e., $l=N-Q$. However, this approaching-zero property at $l=22$ is weakened with the decrease of input SNR; especially for the extremely low SNR case, the first approaching-zero point is completely changed to $l=23$, i.e., $l=N-Q+1$.

To realize the detection of the first approaching-zero point, we can set a small threshold for the judgment, and the search problem can be established as follows:

$$\min_{l=1,...,N} l \quad \text{s.t. } d(l)<\rho \tag{26}$$

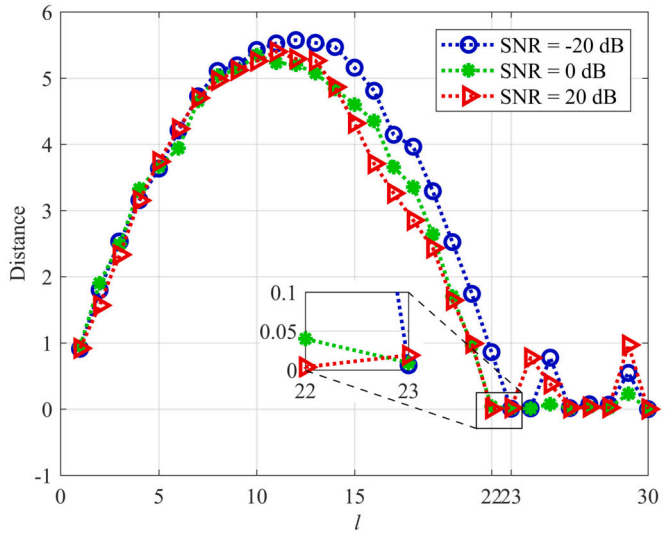

Fig. 2. Distance versus l under three SNR cases (SNR = −20 dB, SNR = 0 dB and SNR = 20 dB).

where ρ is a positive threshold and is close to 0; once (26) is solved with the solution $\hat{l}$, a dimension of QSS can be determined as

$$\hat{Q} = N - \hat{l} \tag{27}$$

Regarding the value of $\hat{Q}$, let Event 1 (E_1) and Event 2 (E_2) represent the events $\hat{Q} = Q$ and $\hat{Q} = Q - 1$, respectively. Clearly, if the small threshold ρ is chosen effectively, that is, within the value range

$$b_L < \rho \leqslant b_U \tag{28}$$

where the lower bound b_L and upper bound b_U are

$$b_L = \min\left\{d\left(N-Q\right), d\left(N-Q+1\right)\right\}, \tag{29}$$

$$b_U = \min\left\{d\left(k\right),\ k = 1, ..., N-Q-1\right\}, \tag{30}$$

respectively, E_1 and E_2 satisfy $E_1 \cup E_2 = \Omega$, where Ω is the entire event space. Under such a premise, the result can be achieved as expected, that is $\hat{Q} = \bar{Q}$, where

$$\bar{Q} = \begin{cases} Q, & d\left(N-Q\right) < \rho \\ Q-1, & d\left(N-Q+1\right) < \rho \leqslant d\left(N-Q\right) \end{cases} \tag{31}$$

It should be mentioned that since $b_U \gg b_L \approx 0$ as described in the previous remarks, the effective threshold satisfying (28) is not difficult to determine to some extent.

In this study, the QSS is still constructed based on partial eigenvectors of the SCM as general. Thereupon, performing eigendecomposion for the SCM $\hat{\mathbf{R}}$ yields

$$\hat{\mathbf{R}} = \mathbf{U}\mathbf{\Lambda}\mathbf{U}^H \tag{32}$$

where the diagonal matrix $\mathbf{\Lambda}$ contains the eigenvalues of $\hat{\mathbf{R}}$ in a descending order, the unitary matrix $\mathbf{U}$ contains the corresponding eigenvectors. The orthogonal bases of the QSS $\langle \mathbf{U}_D \rangle$ can be chosen by taking the first $\hat{Q}$ eigenvectors of $\mathbf{U}$, denoted as

$$\mathbf{U}_D = \mathbf{U}_{[\hat{Q}]} \tag{33}$$

Here, given the small threshold ρ satisfying (28), the dimension of $\langle \mathbf{U}_D \rangle$ would be selected as Q in the high SNR case pointed out in 3.1.1, so $\langle \mathbf{U}_D \rangle$ is the signal subspace corresponding to the SCM in such a case. On the other hand, in the relatively low SNR case pointed out in 3.1.2, especially when severe subspace leakage happens, the dimension of $\langle \mathbf{U}_D \rangle$ is likely to be changed to $Q-1$, therefore $\langle \mathbf{U}_D \rangle$ is estimated as a non-complete sample signal subspace (or the sample interference subspace). As we can observe, with an effective threshold, regardless of either case discussed above, the estimated QSS $\langle \mathbf{U}_D \rangle$ can contain all the components of actual interference SVs while isolating the noise components approximately. This property of $\mathbf{U}_D$ is valuable for the estimation of relevant factors of interference in the INCM reconstruction.

3.2. Interference steering vector and power estimation

It is readily known that the classical multiple signals classification (MUSIC) algorithm is provided to estimate the directions of the signals according to the orthogonality between the SVs of the signals and the noise subspace. Since the QSS has been estimated, we intend to estimate the interference DOAs with a MUSIC-like method. Similar to the conventional MUSIC spatial spectrum which is described as $P_{\mathrm{MUSIC}}(\theta) = 1/\left|\mathbf{a}^H(\theta)\mathbf{U}_n\mathbf{U}_n^H\mathbf{a}(\theta)\right|$, the proposed spectral estimator is defined as

$$\hat{P}(\theta) = \frac{1}{\left|\mathbf{a}^H(\theta)\bar{\mathbf{U}}_D\bar{\mathbf{U}}_D^H\mathbf{a}(\theta)\right|} \tag{34}$$

where $\langle \bar{\mathbf{U}}_D \rangle$ is the orthogonal complement space of $\langle \mathbf{U}_D \rangle$. As we analyzed above, the actual interference SVs must lie in the QSS. Under the assumption that the SV mismatch is not significant, we have $\left|\mathbf{a}^H(\theta_i)\bar{\mathbf{U}}_D\bar{\mathbf{U}}_D^H\mathbf{a}(\theta_i)\right| \approx 0,\ i = 1, ..., N - \hat{l}$. Hence, it is feasible to apply (34) to estimate the interference DOAs. From the P peaks outside the region of the SOI angular sector Θ, we can get the interference DOAs as $\{\bar{\theta}_1, \bar{\theta}_{2,...,}\bar{\theta}_P\}$. Then, the nominal interference SVs can be estimated as

$$\bar{\mathbf{a}}_i = \mathbf{a}\left(\bar{\theta}_i\right), i = 1, ..., P \tag{35}$$

Since the nominal interference SVs are estimated based on the perfect array manifold, the estimates in (35) may be inaccurate if the array perturbations exist. To alleviate this problem, we adopt the subspace projection theory to modify the interference SV estimates. By employing the QSS $\mathbf{U}_D$ once again, the interference SV can be further estimated as

$$\hat{\mathbf{a}}_i = \mu_i\mathbf{U}_D\mathbf{U}_D^H\bar{\mathbf{a}}_i,\ i = 1, ..., P \tag{36}$$

Here, the scalar $\mu_i = \sqrt{N}/\left\|\mathbf{U}_D\mathbf{U}_D^H\bar{\mathbf{a}}_i\right\|$ is set to make the estimated and presumed interference SV norms coincide, which can avoid the scaling ambiguity problem as mentioned in [15]. To proceed, according to (36), the interference power can be estimated based on the Capon spectrum. Here, we substitute the estimated interference SV $\hat{\mathbf{a}}_i$ into (13), then the power of ith interference can be calculated as follows:

$$\begin{aligned} \hat{\sigma}_i^2 &= \frac{1}{\hat{\mathbf{a}}_i^H\hat{\mathbf{R}}^{-1}\hat{\mathbf{a}}_i} \\ &= \frac{1}{\left(\mu_i\mathbf{U}_D\mathbf{U}_D^H\bar{\mathbf{a}}_i\right)^H\hat{\mathbf{R}}^{-1}\left(\mu_i\mathbf{U}_D\mathbf{U}_D^H\bar{\mathbf{a}}_i\right)} \\ &= \frac{1}{\mu_i^2}\left(\frac{1}{\bar{\mathbf{a}}_i^H\mathbf{U}_D\mathbf{\Lambda}_D^{-1}\mathbf{U}_D^H\bar{\mathbf{a}}_i}\right) \end{aligned} \tag{37}$$

It worth noting that the subspace-based power estimation scheme for SOI in [43,44] is $\hat{\delta}_0^2 = 1/\bar{\mathbf{a}}_0^H\mathbf{U}_S\mathbf{\Lambda}_S^{-1}\mathbf{U}_S^H\bar{\mathbf{a}}_0$; if it is borrowed to estimate the interference power with the replacement of $\bar{\mathbf{a}}_i$ for $\bar{\mathbf{a}}_0$, the corresponding power estimation scheme for the ith interference can be formed as $\hat{\delta}_i^2 = 1/\bar{\mathbf{a}}_i^H\mathbf{U}_S\mathbf{\Lambda}_S^{-1}\mathbf{U}_S^H\bar{\mathbf{a}}_i$. Interestingly, it can be observed that the estimate in (37) replaces the signal subspace $\langle \mathbf{U}_S \rangle$ with an estimated QSS, and produces a coefficient $1/\mu_i^2$ additionally.

3.3. Noise power estimation

In practical applications, noise power can be measured in advance. For the reduction of the prior knowledge, some RAB methods serve the minimum eigenvalue of the SCM as a substitute for the practical noise power, but in low snapshots, this value may be underestimated

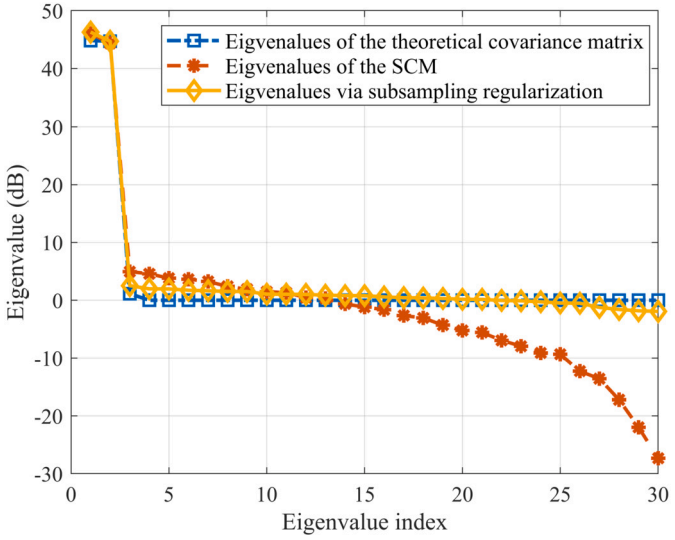

Fig. 3. Comparison of eigenvalues of different covariance matrices.

too much due to the effect of noise eigenvalue dispersion [6]. Thus, some other methods use the average of subdominant sample eigenvalues as an alternative. For all that, it needs to know the source number for a prior or select an empirical value as the threshold to distinguish between noise eigenvalues and signal eigenvalues. To obtain a more precise estimate of noise power with less prior knowledge, we present a novel method taking advantage of the subsample eigenvectors. In the previous work in [10], a modified eigenvalue matrix with less noise spread for the SCM $\hat{\mathbf{R}}$ can be calculated as

$$\tilde{\mathbf{\Lambda}} = \operatorname{diag}\left(\mathbf{U}_1^H \hat{\mathbf{R}}_2 \mathbf{U}_1\right) \tag{38}$$

By adopting the independent and identically distributed property of noise in the time domain, the nonlinear regularization process in (38) has been demonstrated to reduce the subdominant eigenvalues (or noise eigenvalues) spread with great potential. Thus, we can apply the minimum diagonal element of $\tilde{\mathbf{\Lambda}}$ as the estimate of the noise power, yielding that:

$$\hat{\sigma}_{\mathrm{n}}^2 = \hat{\mathbf{u}}_{1N}^H \hat{\mathbf{R}}_2 \hat{\mathbf{u}}_{1N} \tag{39}$$

To measure the feasibility of (39), we display the re-estimated eigenvalues in (39) along with the eigenvalues of the theoretical covariance matrix and the SCM, where a simulation scenario with a 30-element ULA, two incident signals and 30 sampling snapshots is considered. The number of subsampling snapshots is taken as $J = 15$.

It can be seen from Fig. 3 that the noise eigenvalue spread of $\tilde{\mathbf{\Lambda}}$ is substantially less than $\mathbf{\Lambda}$, so it is more reliable to take the minimum diagonal element of $\tilde{\mathbf{\Lambda}}$ as the estimate of the noise power. Then, the INCM is reconstructed as follows:

$$\hat{\mathbf{R}}_{\mathrm{i+n}} = \hat{\sigma}_{\mathrm{n}}^2 \mathbf{I}_N + \sum_{i=1}^{P} \hat{\sigma}_i^2 \hat{\mathbf{a}}_i \hat{\mathbf{a}}_i^H \tag{40}$$

To avoid redundant operations in (40), let (36) and (37) be substituted into (40); the reconstructed INCM can be calculated in a more efficient form as

$$\hat{\mathbf{R}}_{\mathrm{i+n}} = \hat{\sigma}_{\mathrm{n}}^2 \mathbf{I}_N + \sum_{i=1}^{P} \frac{\mathbf{U}_{\mathrm{D}} \mathbf{U}_{\mathrm{D}}^H \bar{\mathbf{a}}_i \bar{\mathbf{a}}_i^H \mathbf{U}_{\mathrm{D}} \mathbf{U}_{\mathrm{D}}^H}{\bar{\mathbf{a}}_i^H \mathbf{U}_{\mathrm{D}} \mathbf{\Lambda}_{\mathrm{D}}^{-1} \mathbf{U}_{\mathrm{D}}^H \bar{\mathbf{a}}_i} \tag{41}$$

Comparing (41) with (40), we can observe that the separate calculations of interference SVs and powers have been omitted in the reconstruction.

3.4. Signal-of-interest steering vector estimation and weight vector computation

The general strategy of the SVE is to maximize the output power while preventing the estimate from converging to the interference SVs or their combinations. In this work, we still follow this strategy to estimate the SOI SV.

$$P = \frac{1}{\left(\bar{\mathbf{a}}_0 + \mathbf{e}\right)^H \hat{\mathbf{R}}^{-1} \left(\bar{\mathbf{a}}_0 + \mathbf{e}\right)} \tag{42}$$

The objective of the optimization problem can be established by maximizing the output power, i.e., minimizing the denominator of (42). Since the INCM has been reconstructed by (41), we can use the idea of [19,34] to set the constraint to prevent the estimate from converging to the interference SVs or their combinations. The optimization problem of estimating the SOI SV can be formulated as follows:

$$\begin{aligned} \min_{\mathbf{e}} \quad & \left(\bar{\mathbf{a}}_0 + \mathbf{e}\right)^H \hat{\mathbf{R}}^{-1} \left(\bar{\mathbf{a}}_0 + \mathbf{e}\right) \\ \text{s.t.} \quad & \left(\bar{\mathbf{a}}_0 + \mathbf{e}\right)^H \hat{\mathbf{R}}_{\mathrm{i+n}} \left(\bar{\mathbf{a}}_0 + \mathbf{e}\right) \leqslant \bar{\mathbf{a}}_0^H \hat{\mathbf{R}}_{\mathrm{i+n}} \bar{\mathbf{a}}_0 \end{aligned} \tag{43}$$

Furthermore, the mismatch vector $\mathbf{e}$ is composed of two components, $\mathbf{e}_\perp$ and $\mathbf{e}_{\shortparallel}$, with $\mathbf{e}_\perp$ being orthogonal to $\bar{\mathbf{a}}_0$ and $\mathbf{e}_{\shortparallel}$ being parallel to $\bar{\mathbf{a}}_0$ [19]. The parallel component $\mathbf{e}_{\shortparallel}$ does not affect the SV estimation, and it can be ignored accordingly in (43). Then, the optimization problem of (43) can be transformed as

$$\begin{aligned} \min_{\mathbf{e}_\perp} \quad & \left(\bar{\mathbf{a}}_0 + \mathbf{e}_\perp\right)^H \hat{\mathbf{R}}^{-1} \left(\bar{\mathbf{a}}_0 + \mathbf{e}_\perp\right) \\ \text{s.t.} \quad & \left(\bar{\mathbf{a}}_0 + \mathbf{e}_\perp\right)^H \hat{\mathbf{R}}_{\mathrm{i+n}} \left(\bar{\mathbf{a}}_0 + \mathbf{e}_\perp\right) \leqslant \bar{\mathbf{a}}_0^H \hat{\mathbf{R}}_{\mathrm{i+n}} \bar{\mathbf{a}}_0 \\ & \bar{\mathbf{a}}_0^H \mathbf{e}_\perp = 0 \end{aligned} \tag{44}$$

The above QCQP problem can be solved by the convex optimization toolbox. Subsequently, we can get the estimate of the SOI SV as

$$\hat{\mathbf{a}}_0 = \bar{\mathbf{a}}_0 + \mathbf{e}_\perp \tag{45}$$

Finally, substituting the reconstructed covariance matrix $\hat{\mathbf{R}}_{\mathrm{i+n}}$ and the estimated SOI SV $\hat{\mathbf{a}}_0$ into (7), the weight vector of the proposed adaptive beamformer can be computed as

$$\mathbf{w}_{\mathrm{pro}} = \frac{\hat{\mathbf{R}}_{\mathrm{i+n}}^{-1} \hat{\mathbf{a}}_0}{\hat{\mathbf{a}}_0^H \hat{\mathbf{R}}_{\mathrm{i+n}}^{-1} \hat{\mathbf{a}}_0} \tag{46}$$

3.5. Algorithm summary and computational complexity analysis

In summary, the procedure of the proposed RAB method can be divided into seven steps in Algorithm 1:

Algorithm 1 Proposed RAB Algorithm.

1: Calculate the SCM $\hat{\mathbf{R}} = (1/K)\mathbf{X}\mathbf{X}^H$, along with the two SSCMs $\hat{\mathbf{R}}_1 = (1/J)\mathbf{X}_1\mathbf{X}_1^H$ and $\hat{\mathbf{R}}_2 = \left[1/(K-J)\right]\mathbf{X}_2\mathbf{X}_2^H$.
2: Eigen-decompose the SCM $\hat{\mathbf{R}}$ and the two SSCMs $\hat{\mathbf{R}}_1$, $\hat{\mathbf{R}}_2$, then rearrange the eigenvectors of $\hat{\mathbf{R}}_1$ and $\hat{\mathbf{R}}_2$ in reverse order, that is, $\mathbf{V}_1 = \mathcal{F}\left(\mathbf{U}_1\right)$, $\mathbf{V}_2 = \mathcal{F}\left(\mathbf{U}_2\right)$.
3: Determine the first approaching-zero point of subspace distance by (26), and obtain a QSS $\langle \mathbf{U}_{\mathrm{D}} \rangle$ via (33).
4: Obtain the nominal interference SVs $\left\{\bar{\mathbf{a}}_1, \bar{\mathbf{a}}_{2,\ldots,}\bar{\mathbf{a}}_P\right\}$ using a MUSIC-like spatial spectrum (34).
5: Estimate the noise power via (39), then reconstruct the INCM via (41).
6: Correct the SOI SV by solving a QCQP problem (44).
7: Compute the ultimate weight vector of the proposed beamformer utilizing the reconstructed INCM $\hat{\mathbf{R}}_{\mathrm{i+n}}$ and estimated SOI SV via (46).

In our approach, the computational complexity mainly consists of three parts: the estimation of the QSS, the reconstruction of INCM and the upgradation of SOI SV. For the part of the estimation of the QSS,

the computational load is mainly caused by the eigen-decompositions and the dimension search. In eigen-decompositions, since there are three covariance matrices (SCM and two SSCMs) required to be eigen-decomposed, the computational complexity is $O\left(3N^3\right)$. In dimension search, the computational complexity comes from the computation of the Grassmann kernel, which is only $O\left(\hat{l}N\right)$. Furthermore, for the part of the reconstruction of INCM, the computational complexity is dominated by the calculation of MUSIC-like spatial spectrum for estimating the nominal interference SVs; suppose that R denotes the number of spatial search points, the computational complexity in the second part is approximately $O\left(\hat{l}RN\right)$. To proceed, for the part of the upgradation of SOI SV, the QCQP problem requires to be solved, which has the complexity of $O\left(N^{3.5}\right)$. Since $R \gg N > \hat{l}$, the overall computational complexity of the proposed reconstruction-based method is approximately $O\left(\max\left(3N^3, \hat{l}RN, N^{3.5}\right)\right)$.

3.6. Selection of relevant parameters

3.6.1. Selection of subsampling dimension J

The subsampling is used in two parts: (a) the estimation of QSS in Section 3.1 and (b) the estimation of noise power in Section 3.3, where the subsampling dimension J is crucial in these two parts.

For the estimation of QSS, the dimension is chosen in terms of the first approaching-zero point of subspace distance, of which the theoretical basis is the signal subspace proximity. Either the SSCM $\hat{\mathbf{R}}_1$ or $\hat{\mathbf{R}}_2$ with lack of subsample snapshots would make the corresponding subsample eigenvectors significantly biased from the true one with high probability. This may reduce the signal subspace proximity, making the distance with respect to $\hat{l}$ approach zero inconspicuously. Hence, as a trade-off decision, we can make the dimensions of the two SSCMs identical if possible. For such a choice of J, on the other hand, can make the distributions of the eigenvectors of $\hat{\mathbf{R}}_1$ and $\hat{\mathbf{R}}_2$ to be the same, thus it may be more convenient to study the statistical behavior of $d(l)$ accordingly. Based on the discussion above, we can take the subsample number of the first subsample as the integer value rounded to $K/2$, i.e., $J = \text{round}(K/2)$ for this use. (Considering K may be an odd number, we take the rounding operation).

In addition, J is also important for the nonlinear regularization process adopted for the noise power estimation. It has been demonstrated in [10] that if the value of J is taken as an integer within the range $J \in [\max(Q, 0.2K), K - \max(Q, 0.2K)]$, this subsampling estimator can achieve a stable performance for improving the regularization effect of SCM with random noise components and the estimation of noise power as well. In this study, we suppose that the number of snapshots is far greater than the source number, i.e., $K \gg Q$; under this assumption, the choice of J discussed in the preceding paragraph is also located in such a set, thus also suitable for the estimation of noise power.

Overall, for a reliable choice, the parameter J can be chosen as $J = \text{round}(K/2)$ in this study.

3.6.2. Rough selection of threshold ρ for first approaching-zero point and remedy for an extreme case

It can be noticed that the exact statistical behavior of $d(l)$ is, in practice, too complicated to offer valuable insight for determining a suitable range for the threshold. For all that, we can roughly find out the trend of $d(l)$ versus l in Fig. 2; the general trend can be described as increasing first and then decreasing until arriving at the first approaching-zero point; thus, the vital referenced points for determining the upper bound of ρ are $d(1)$ and $d\left(N - \bar{Q} - 1\right)$. From Appendix B, $d(1), d\left(N - \bar{Q} - 1\right) \approx 1$; hence, a rough upper bound for ρ is 1. Considering the sample size is finite, the range of effective threshold should be narrowed down from $(0, 1]$; furthermore, with respect to beamformer output performance, the value taken for ρ can be further refined. Additional discussion on the detailed selection of ρ can be found in Section 4.1 in the simulations.

In addition, it is worth noting that, although this study does not consider interference-free or weak-interference scenarios, an extreme case of missed interference detection may occur as a result of an ineffective setting of ρ. Given that both $\left\langle \mathbf{V}_{1,[N]} \right\rangle$ and $\left\langle \mathbf{V}_{2,[N]} \right\rangle$ are the entire space, it follows that $d(N) \equiv 0$. If ρ is artificially set too small, falling below the lower bound, the search result from (26) may be $\hat{l} = N$, resulting in $\hat{Q} = 0$. In such an extreme case, where interference sources go undetected, Eq. (33) becomes meaningless, and subsequent steps cannot proceed. To remedy this issue, one possible solution is to accept the incorrect estimation result $\hat{Q} = 0$ and assign the ultimate weight vector as $\mathbf{w}_{\text{pro}} = \bar{\mathbf{a}}_0$, i.e., the classical delay-and-sum beamformer, which can serve as a viable alternative for the interference-free scenarios

4. Simulation results

In the numerical experiments, we first address the determination of the threshold ρ for the proposed method in Section 4.1. Subsequently, in Section 4.2, the proposed method is compared with several existing RAB methods. The studied array is a uniform linear array with $N = 10$ identical isotropic sensors spaced half a wavelength apart. The additive noise is assumed to be spatially white Gaussian with unit variance. Besides, the SOI is presumed to arrive at the array from a nominal angle of $\theta_0 = 0$, while the interference model is set as stated in the following experiments; all the sources are assumed to be narrowband and uncorrelated with each other. The subsampling dimension J is chosen as $J = \text{round}(K/2)$ for all simulations.

4.1. Determination of ρ for the proposed method

In this subsection, we discuss the determination of the threshold ρ. Since the primary requirement for ρ is to serve as an effective threshold to make $\hat{Q} = \bar{Q}$ as expected, we first examine the probability of the effective threshold with different ρ across a wide range in 4.1.1 Example 1. Following this, we narrow down the range of values, selecting several relatively effective choices for comparison of output performance in 4.1.2 Example 2. This subsection considers two simulation interference scenarios: the first scenario is a single interference source located at $-45°$, while the second is two interference sources located at $\{-45°, 30°\}$. For both the aforementioned scenarios, the INR for each interference source is randomly set between 20 dB and 40 dB in every Monte Carlo trial, with a total of 1000 trials.

4.1.1. Example 1: Effective threshold screening with different ρ across a wide range

In the first example, we examine effective threshold probability as a function of sample size under an ideal case without SV mismatch. From the search order for the first approaching-zero point, or (26), it is easily known that $\hat{Q} = \bar{Q}$ is equivalent to $\hat{Q} = Q \vee Q - 1$, where '$\vee$' denotes logical OR. Thus, here we define the effective threshold probability as follows:

$$P_{\text{e}} = \frac{\text{number of } \hat{Q} = Q \vee Q - 1}{\text{number of total trials}} \tag{47}$$

Based on the rough selection of ρ in Section 3.6.2, we take the choices with a wide range, including $\rho = 0.01, 0.05, 0.1, \text{and } 0.5$.

Fig. 4 and Fig. 5 show P_{e} versus sample size in the scenarios of one interference and two interferences, respectively, where the results of three input SNR cases (SNR $= -20$ dB, SNR $= 0$ dB and SNR $= 20$ dB) are depicted in these two figures. From Fig. 4 and Fig. 5, it can be seen that the two choices $\rho = 0.05$ and $\rho = 0.1$ can almost guarantee the stable estimation of dimension as Q or $Q - 1$ stably, and the choice $\rho = 0.5$ can obtain at least a 94% effective threshold probability. However, the choice $\rho = 0.01$ is relatively ineffective, especially for the sample-starving case ($K = 10$); this is because the property of approaching zero described in (20) and (23) may be significantly weakened in such a case, leading to an increase in the lower bound of the effective threshold.

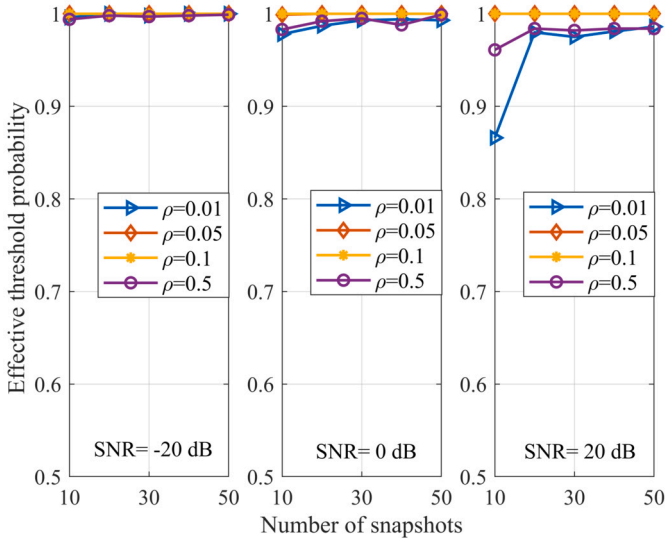

Fig. 4. Effective threshold probability of the proposed method with $\rho = 0.01$, $\rho = 0.05$, $\rho = 0.1$, and $\rho = 0.5$ in the scenario of one interference source.

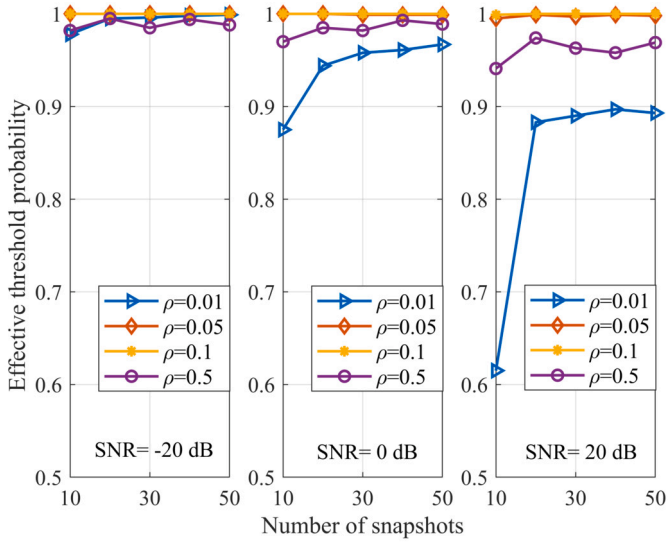

Fig. 5. Effective threshold probability of the proposed method with $\rho = 0.01$, $\rho = 0.05$, $\rho = 0.1$, and $\rho = 0.5$ in the scenario of two interference sources.

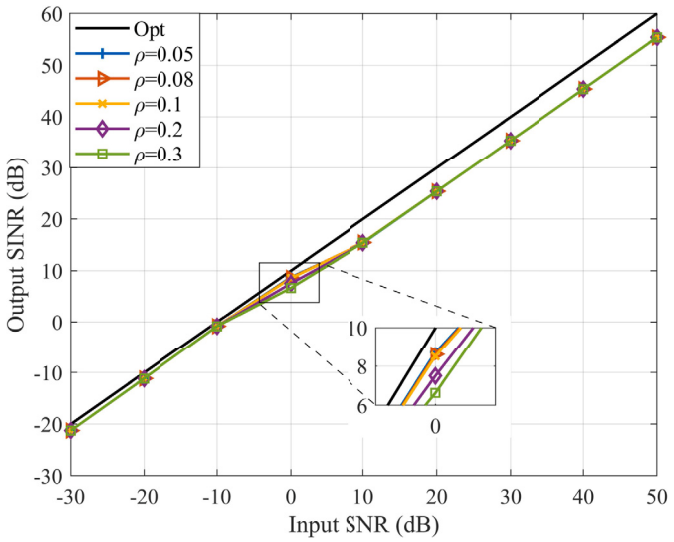

(a) Output SINR versus input SNR

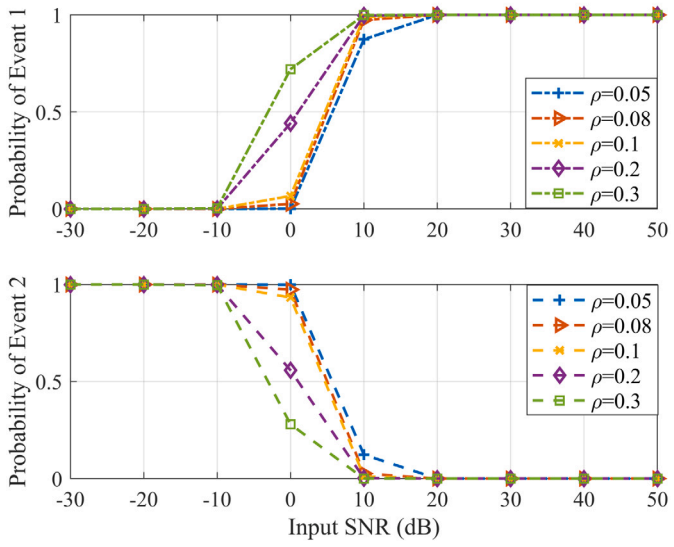

(b) Probabilities of Event 1 and Event 2

Fig. 6. Performance comparison of the proposed method with $\rho = 0.05$, $\rho = 0.08$, $\rho = 0.1$, $\rho = 0.2$, and $\rho = 0.3$ in the scenario of one interference source.

4.1.2. Example 2: Performance comparison with different ρ across a narrow range

In the second example, we investigate the impact of different choices of ρ on the performance of the proposed method. Based on Example 1, the choices $\rho = 0.01$ and $\rho = 0.5$ are not effective enough to ensure $\hat{Q} = Q \vee Q - 1$, and are therefore discarded. Consequently, we refine the range of ρ to a more effective set of values, specifically $\rho = 0.05, 0.08, 0.1, 0.2,$ and 0.3. Apart from comparing beamformer output SINR versus input SNR, we also indirectly examine the estimated dimensions of the QSS at corresponding SNR points through the probabilities of Event 1 and Event 2, which are defined as follows.

$$P_1 = \frac{\text{number of } \hat{Q} = Q}{\text{number of total trials}} \tag{48}$$

$$P_2 = \frac{\text{number of } \hat{Q} = Q - 1}{\text{number of total trials}} \tag{49}$$

In this example, the SV mismatch caused by random SV error, as described in 4.2.1 Example 1, is considered. The number of snapshots is set as $K = 30$.

The performance comparisons are depicted in Fig. 6 for the scenario of one interference source and in Fig. 7 for the scenario of two interference sources. Fig. 6 (a) and Fig. 7(a) show the output SINR versus input SNR, while the probabilities of Event 1 and Event 2 at each SNR point are drawn in Fig. 6 (b) and Fig. 7 (b). The results indicate that the proposed method is insensitive to ρ under the promise that ρ is a relatively effective threshold. From Fig. 6 (b) and Fig. 7 (b), regardless of the choice of ρ, the estimates of the dimension of the QSS are Q at high SNR levels (SNR $\geqslant$ 20 dB), and $Q - 1$ at extremely low SNR levels (SNR $\leqslant -10$ dB), leading to consistent output SINRs as illustrated in Fig. 6(a) and Fig. 7(a). Moreover, at two moderate-low SNR points, SNR = 0 dB and SNR = 10 dB, the estimates may fluctuate. Particularly, at SNR = 0 dB, a smaller ρ value (e.g. 0.05, 0.08 or 0.1) tends to favor the estimate $\hat{Q}$ being $Q - 1$ over Q, and possess better output performance than that of a larger ρ value (e.g. 0.2 or 0.3) as shown in Fig. 6 (b) and Fig. 7 (b).

Overall, we find that $\rho = 0.1$ is a favorable choice and, thus, adopted in the upcoming experiments.

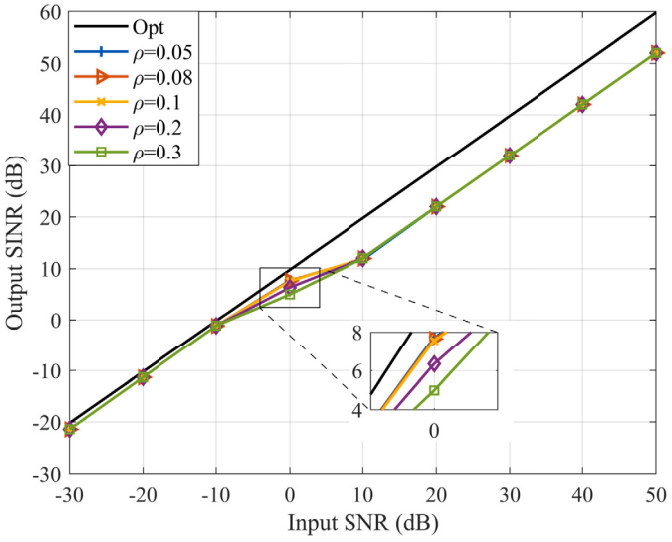

(a) Output SINR versus input SNR

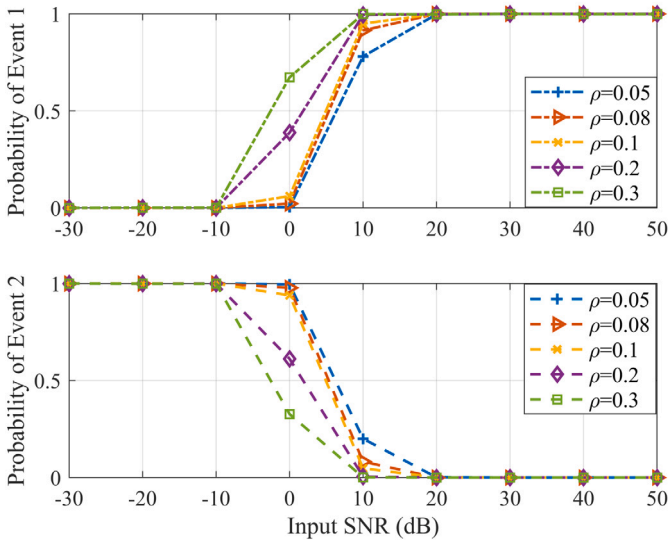

(b) Probabilities of Event 1 and Event 2

Fig. 7. Performance comparison of the proposed method with $\rho = 0.05$, $\rho = 0.08$, $\rho = 0.1$, $\rho = 0.2$, and $\rho = 0.3$ in the scenario of two interference sources.

4.2. Performance comparison with RAB methods

In this section, the proposed method is compared with several existing RAB methods, two interference sources are considered to be nominally located at $\{\theta_1, \theta_2\} = \{-45°, 30°\}$, with the input INRs equal to INR = 20 dB and INR = 30 dB, respectively. For each simulation run, the number of snapshots is set to 30 as the input SNR varies, while the input SNR is fixed at 20 dB as the number of snapshots varies. 200 Monte-Carlo trials are conducted for each case.

The compared beamformers include the robust Capon beamformer (RCB) [15], the INCM reconstruction beamformers based on different techniques: QCQP (INCM-QCQP) [19], subspace projection (INCM-SUB) [20], MEPS (INCM-MEPS) [21], covariance matrix diagonal loading (INCM-CDL) [30], unwanted signal removal and Gauss-Legendre quadrature (INCM-URGLQ) [34], and SV error neighborhood table search (INCM-ENTS) [36], where the simulation parameters are set as follow:

1) The SOI uncertainty set parameter in the RCB is set as $\varepsilon_S = 3$;
2) For the INCM-QCQP and INCM-SUB, the defined angular sector for each source (SOI or interference) is taken as $[\theta_i - 5°, \theta_i + 5°]$, $i = 0, 1, 2$;
3) For the INCM-CDL, the loading trigger threshold is fixed at $\mu = 16$ dB;
4) For the INCM-ENTS, the four parameters of the SV error neighborhood table are set as those in the original study [36].

In all simulations, the optimal output SINR is calculated by

$$\mathrm{SINR}_{\mathrm{opt}} = \sigma_0^2 \mathbf{a}_0^H \mathbf{R}_{\mathrm{i+n}}^{-1} \mathbf{a}_0 \tag{50}$$

4.2.1. Example 1: Mismatch due to random SV error

In the first example, the random SV mismatch is considered. The actual SVs of the SOI and interference are generated randomly as follows:

$$\mathbf{a}_i = \bar{\mathbf{a}}_i + \mathbf{e}_i, \ i = 0, ..., Q \tag{51}$$

where $\bar{\mathbf{a}}_i$ represents the nominal SV of ith signal corresponding to θ_i. $\mathbf{e}_i$ denotes the SV error vector of ith signal, which is modeled as follows

$$\mathbf{e}_i = \frac{\varepsilon_i}{\sqrt{N}} \left[e^{j\varphi_{i,1}}, e^{j\varphi_{i,2}}, ..., e^{j\varphi_{i,N}} \right]^T \tag{52}$$

where ε_i denotes the norm of the error vector $\mathbf{e}_i$, satisfying the uniform distribution $\left[0, \sqrt{0.3}\right]$, while $\varphi_{i,n}, n = 1, ..., N$ represents the phase of $\mathbf{e}_i$, satisfying the uniform distribution $[0, 2\pi)$.

Fig. 8(a) and Fig. 8(b) display the output SINR versus input SNR and the number of snapshots of different RAB methods, respectively. The two figures show that the proposed method performs better than other beamformers for comparison. Specifically, from Fig. 8(a), it can be observed that when the input SNR is less than 10 dB, the output SINR of the proposed method and the INCM-CDL is prominently larger than that of other reconstruction-based methods. For the case SNR > 10 dB, the proposed methods outperform the RCB and the INCM-CDL. Moreover, as seen from Fig. 8(b), the performances of all reconstruction-based methods except the INCM-CDL fluctuate slightly when the number of snapshots varies, while the proposed algorithm and INCM-ENTS have the most stable performance, especially when the number of snapshots is less than 30; this owes to the precise estimate of each vital factor in the process of INCM reconstruction in our approach.

4.2.2. Example 2: Mismatch due to look direction error

In the second simulation example, we study the impact due to the random look direction error. For each simulation run, the look direction errors of both the SOI and interference are assumed to be uniformly distributed in $[-4°, 4°]$.

Fig. 9(a) evaluates the output SINR versus the input SNR. It can be seen due to the SOI component present in the SCM, the robustness of the RCB (sample-based RAB method) and INCM-CDL decreases significantly with the increase of input SNR. Additionally, as the interference power is strong, the performance of the INCM-URGLQ is not perfect enough when random interference look direction errors exist. In contrast, the proposed methods can gain satisfactory performance as the rest of the reconstruction-based methods. Especially when the input SNR is strong enough to exceed 10 dB, the output SINR of the proposed method almost coincides with the optimal value. To proceed, Fig. 9(b) depicts the output SINR versus the number of snapshots. We can observe that the proposed method, the INCM-SUB and the INCM-ENTS, can obviously obtain better performance than other methods in the entire range.

4.2.3. Example 3: Mismatch due to look direction error and gain and phase errors

In the third simulation example, the scenario of SV mismatch due to look direction error along with gain and phase errors is investigated. The nth element of the actual SV corresponding to the ith signal $(i = 0, 1, 2)$ is modeled as $(1 + \Delta g_n) e^{j\Delta\varphi_n} e^{j(2\pi/\lambda)[(n-1)d]\sin(\theta_i + \Delta\theta)}$, where the look direction error $\Delta\theta$ is set as that in Example 2, the gain error Δg_n is assumed to be independent and identically distributed zero-

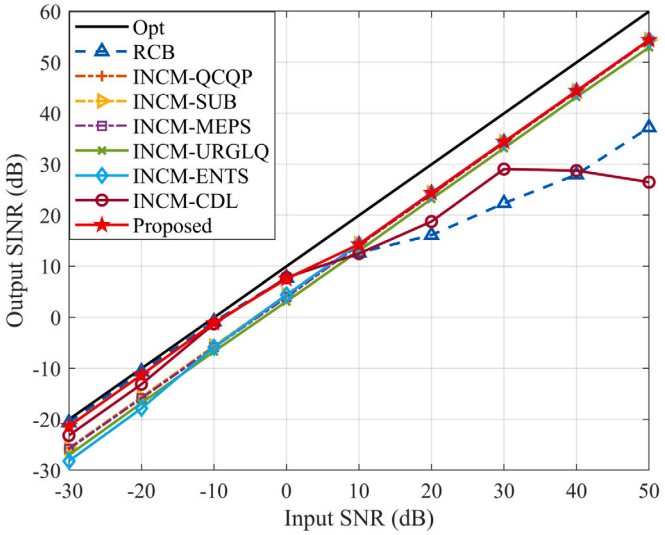

(a) Output SINR versus input SNR, $K = 30$

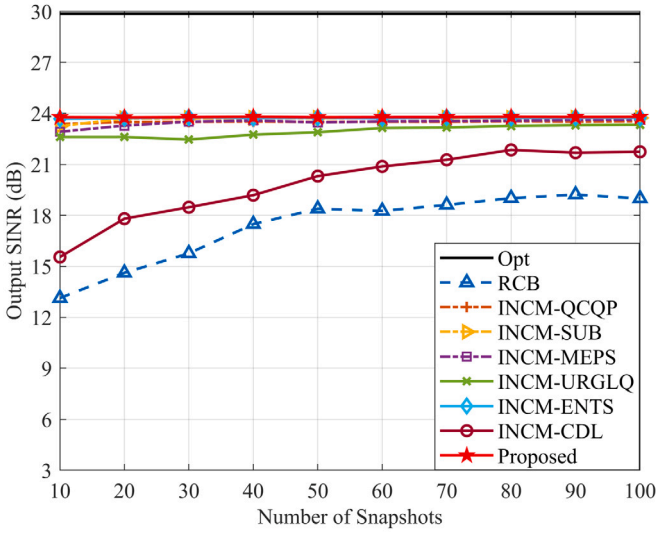

(b) Output SINR versus number of snapshots, input SNR = 20 dB

Fig. 8. Performance comparison in the case of SV random error.

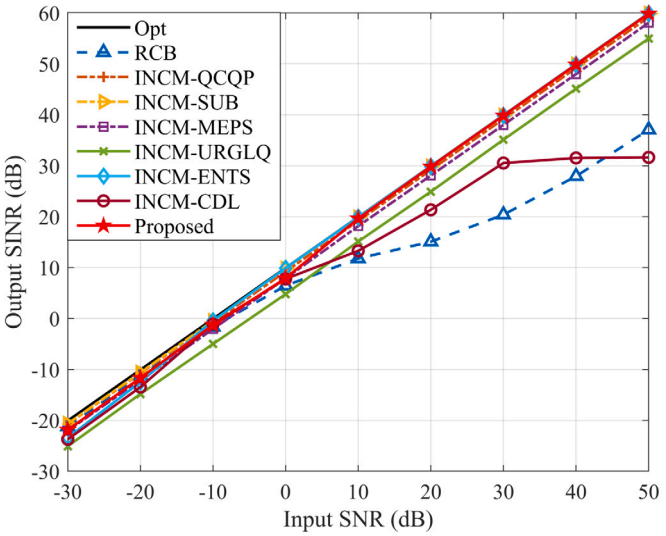

(a) Output SINR versus input SNR, $K = 30$

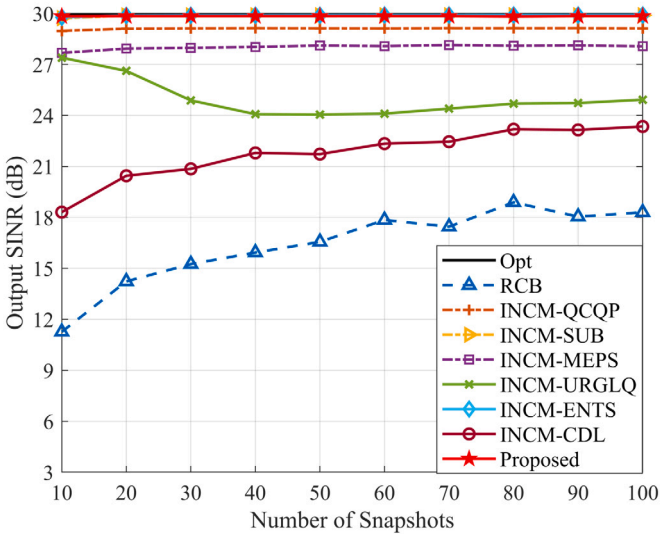

(b) Output SINR versus number of snapshots, input SNR = 20 dB

Fig. 9. Performance comparison in the case of look direction error.

mean Gaussian random variables with the standard derivation 0.05. The phase error $\Delta\varphi_n$ is assumed to be independent and uniformly distributed in $[-5°, 5°]$.

Fig. 10(a) reveals the performance curves versus the input SNR, while the performance curves versus the number of snapshots are drawn in Fig. 10(b). Fig. 10(a) illustrates that the proposed method can still possess good performance in the whole input SNR range as compared with other RAB methods. Since the array perturbations are considered in this example, most of the reconstruction-based methods acquire SINR reduction at low SNR; this is because the imprecise estimates of the interference SVs in the reconstructed INCM restrict the anti-interference ability of the beamformers. Despite all this, the proposed reconstruction-based method presents a novel scheme for estimating the INCM, making the performance as good as the RCB at low SNR when the gain and phase errors exist. In addition, from Fig. 10(b), it is straightforward to see that the proposed method has the best convergence than other methods for comparison, or in other words, the proposed method is applicable under small training size in such a simulation example.

4.2.4. *Example 4: Mismatch due to look direction error and sensor location error*

In the fourth example, the impact of sensor displacement on the performance of beamformers is examined. The nth SV element is model as $e^{j(2\pi/\lambda)[(n-1)d+\Delta d_n]\sin(\theta_0+\Delta\theta)}]$, where the look direction error $\Delta\theta$ is set as it in the above two examples, the sensor location error Δd_n is uniformly drawn from the $[-0.05, 0.05]$ measured in wavelengths. Likewise, Fig. 11(a) assesses the output SINR versus the input SNR. In view of the existence of the sensor location error, the devised method can still obtain superior performance across the whole range of input SNR. Like the previous example, the INCM-QCQP, INCM-SUB, INCM-MEPS, INCM-URGLQ and INCM-ENTS are not flexible enough to increase their output SINR at low SNR due to the incomplete interference rejections. The INCM-CDL, employing the component of the SCM for the reconstruction, can enjoy performance improvement at low SNR to some extent, but the artificial loading operation is unable to make its performance as good as other reconstruction-based approaches at high SNR levels. Fig. 11(b) simulates the output SINR versus the number of snapshots of different RAB methods. It can be seen from Fig. 11(b) that the provided method is the best and most stable performing one among all

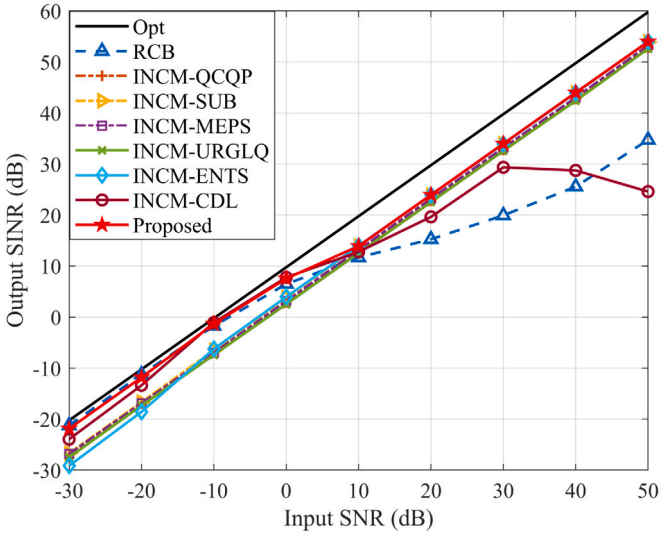

(a) Output SINR versus input SNR, $K = 30$

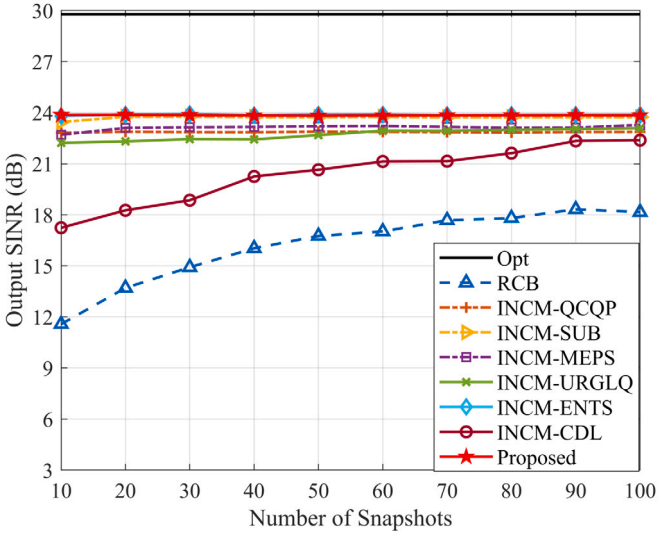

(b) Output SINR versus number of snapshots, input SNR = 20 dB

Fig. 10. Performance comparison in the case of look direction error and gain and phase errors.

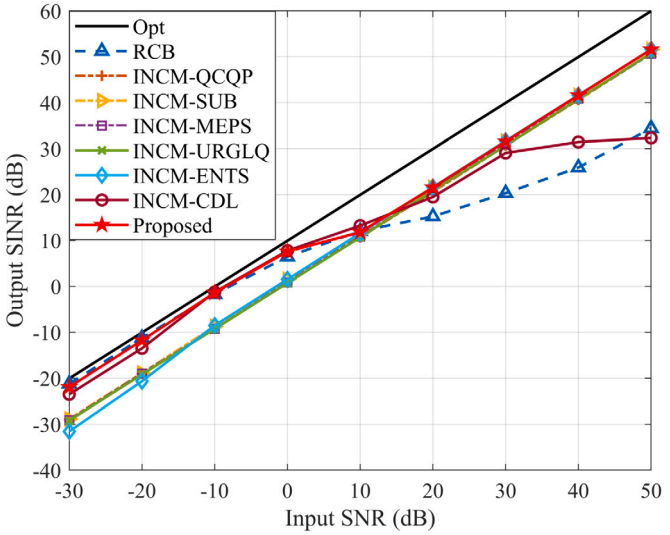

(a) Output SINR versus input SNR, $K = 30$

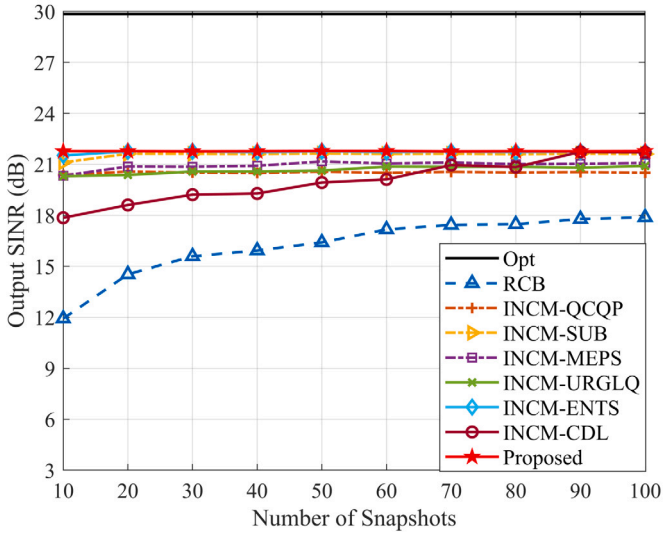

(b) Output SINR versus number of snapshots, input SNR = 20 dB

Fig. 11. Performance comparison in the case of look direction error and sensor location error.

RAB methods in the entire range of snapshot counts. Moreover, the developed method can possess enough robustness under the condition of finite training sample snapshots as before.

5. Conclusion

In this article, a reconstruction-based RAB method based on a novel subspace scheme has been introduced. In this method, a new insight for the selection of QSS dimension through the judgment of subsample subspace distance has been given. Subsequently, the INCM is reconstructed by estimating relevant factors based on the obtained QSS and subsamples. The proposed method is versatile to cope with various types of model errors. Simulation results have shown that the proposed robust adaptive beamformer outperforms the other compared beamformers; significantly, it can prominently improve the performance at low SNR for the reconstruction-based RAB methods if the array is not perfectly calibrated.

However, the threshold for the first approaching-zero point is distinguished empirically to some extent in this study. Future studies will focus on the statistical distribution of the subspace distance in different cases. Thus, the setting of the threshold can be more persuasive.

CRediT authorship contribution statement

Xiangwei Chen: Conceptualization, Investigation, Methodology, Software, Visualization, Writing – original draft, Writing – review & editing. **Weixing Sheng:** Conceptualization, Formal analysis, Supervision, Writing – review & editing.

Declaration of competing interest

The authors declare that they have no known competing financial interests or personal relationships that could have appeared to influence the work reported in this paper.

Data availability

Data will be made available on request.

Acknowledgment

This work was supported in part by the National Natural Science Foundation of China under Grant 62001227 and Grant 62001230.

Appendix A

According to the definition in (17), the subspace distance between $\langle \bar{\mathbf{U}}_{\mathrm{A}} \rangle$ and $\langle \bar{\mathbf{U}}_{\mathrm{B}} \rangle$ is

$$\begin{aligned} d\left(\bar{\mathbf{U}}_{\mathrm{A}}, \bar{\mathbf{U}}_{\mathrm{B}}\right) &= 2^{-1} \left\| \bar{\mathbf{U}}_{\mathrm{A}} \bar{\mathbf{U}}_{\mathrm{A}}^{H} - \bar{\mathbf{U}}_{\mathrm{B}} \bar{\mathbf{U}}_{\mathrm{B}}^{H} \right\|_{F}^{2} \\ &= M - m - \left\| \bar{\mathbf{U}}_{\mathrm{A}}^{H} \bar{\mathbf{U}}_{\mathrm{B}} \right\|_{F}^{2}, m = 1, ..., M \end{aligned} \tag{A.1}$$

The orthogonal complement subspaces $\langle \bar{\mathbf{U}}_{\mathrm{A}} \rangle$ and $\langle \bar{\mathbf{U}}_{\mathrm{B}} \rangle$ satisfy

$$\bar{\mathbf{U}}_{\mathrm{A}} \bar{\mathbf{U}}_{\mathrm{A}}^{H} = \mathbf{I}_{M} - \mathbf{U}_{\mathrm{A}} \mathbf{U}_{\mathrm{A}}^{H} \tag{A.2}$$

$$\bar{\mathbf{U}}_{\mathrm{B}} \bar{\mathbf{U}}_{\mathrm{B}}^{H} = \mathbf{I}_{M} - \mathbf{U}_{\mathrm{B}} \mathbf{U}_{\mathrm{B}}^{H} \tag{A.3}$$

Then, the term of Grassmann kernel in (A.1) can be derived as

$$\begin{aligned} \left\| \bar{\mathbf{U}}_{\mathrm{A}}^{H} \bar{\mathbf{U}}_{\mathrm{B}} \right\|_{F}^{2} &= \mathrm{Tr}\left(\bar{\mathbf{U}}_{\mathrm{A}} \bar{\mathbf{U}}_{\mathrm{A}}^{H} \bar{\mathbf{U}}_{\mathrm{B}} \bar{\mathbf{U}}_{\mathrm{B}}^{H} \right) \\ &= \mathrm{Tr}\left(\left(\mathbf{I}_{M} - \mathbf{U}_{\mathrm{A}} \mathbf{U}_{\mathrm{A}}^{H} \right) \left(\mathbf{I}_{M} - \mathbf{U}_{\mathrm{B}} \mathbf{U}_{\mathrm{B}}^{H} \right) \right) \\ &= \mathrm{Tr}\left(\mathbf{I}_{M} - \mathbf{U}_{\mathrm{A}} \mathbf{U}_{\mathrm{A}}^{H} - \mathbf{U}_{\mathrm{B}} \mathbf{U}_{\mathrm{B}}^{H} + \mathbf{U}_{\mathrm{A}} \mathbf{U}_{\mathrm{A}}^{H} \mathbf{U}_{\mathrm{B}} \mathbf{U}_{\mathrm{B}}^{H} \right) \\ &= \mathrm{Tr}\left(\mathbf{I}_{M} \right) - \mathrm{Tr}\left(\mathbf{U}_{\mathrm{A}} \mathbf{U}_{\mathrm{A}}^{H} \right) - \mathrm{Tr}\left(\mathbf{U}_{\mathrm{B}} \mathbf{U}_{\mathrm{B}}^{H} \right) + \mathrm{Tr}\left(\mathbf{U}_{\mathrm{A}} \mathbf{U}_{\mathrm{A}}^{H} \mathbf{U}_{\mathrm{B}} \mathbf{U}_{\mathrm{B}}^{H} \right) \\ &= M - 2m + \left\| \mathbf{U}_{\mathrm{A}}^{H} \mathbf{U}_{\mathrm{B}} \right\|_{F}^{2} \end{aligned} \tag{A.4}$$

Substituting (A.4) into (A.1), yields

$$\begin{aligned} d\left(\bar{\mathbf{U}}_{\mathrm{A}}, \bar{\mathbf{U}}_{\mathrm{B}}\right) &= M - m - \left(M - 2m + \left\| \mathbf{U}_{\mathrm{A}}^{H} \mathbf{U}_{\mathrm{B}} \right\|_{F}^{2} \right) \\ &= m - \left\| \mathbf{U}_{\mathrm{A}}^{H} \mathbf{U}_{\mathrm{B}} \right\|_{F}^{2} \\ &= d\left(\mathbf{U}_{\mathrm{A}}, \mathbf{U}_{\mathrm{B}} \right) \end{aligned} \tag{A.5}$$

Appendix B

The subspace distance with respect to $l = 1$ is

$$\begin{aligned} d(1) &= 1 - \left\| \mathbf{V}_{1,[1]}^{H} \mathbf{V}_{2,[1]} \right\|_{F}^{2} \\ &= 1 - \left\| \mathbf{u}_{1N}^{H} \mathbf{u}_{2N} \right\|^{2} \end{aligned} \tag{B.1}$$

Since the two noise eigenvectors $\mathbf{u}_{1N}$ and $\mathbf{u}_{2N}$ are nearly independent with each other, we have

$$\left\| \mathbf{u}_{1N}^{H} \mathbf{u}_{2N} \right\|^{2} \approx 0 \tag{B.2}$$

Accordingly, the value of $d(1)$ is approximately 1, i.e.,

$$d(1) \approx 1 \tag{B.3}$$

Subsequently, we discuss the subspace distance with respect to $l = N - \bar{Q} - 1$. According to Theorem 1, the subspace distance with regard to orthogonal complement subspaces can be utilized at this point, which follows that:

$$\begin{aligned} d\left(N - \bar{Q} - 1\right) &= d\left(\mathbf{V}_{1,[N-\bar{Q}-1]}, \mathbf{V}_{2,[N-\bar{Q}-1]} \right) \\ &= d\left(\mathbf{U}_{1,[\bar{Q}+1]}, \mathbf{U}_{2,[\bar{Q}+1]} \right) \end{aligned} \tag{B.4}$$

where

$$d\left(\mathbf{U}_{1,[\bar{Q}+1]}, \mathbf{U}_{2,[\bar{Q}+1]} \right) = \bar{Q} + 1 - \left\| \mathbf{U}_{1,[\bar{Q}+1]}^{H} \mathbf{U}_{2,[\bar{Q}+1]} \right\|_{F}^{2} \tag{B.5}$$

Further, in (B.5), the term $\mathbf{U}_{1,[\bar{Q}+1]}^{H} \mathbf{U}_{2,[\bar{Q}+1]}$ can be expanded as

$$\begin{aligned} \mathbf{U}_{1,[\bar{Q}+1]}^{H} \mathbf{U}_{2,[\bar{Q}+1]} &= \left[\mathbf{U}_{1,[\bar{Q}]}, \mathbf{u}_{1(\bar{Q}+1)} \right]^{H} \left[\mathbf{U}_{2,[\bar{Q}]}, \mathbf{u}_{2(\bar{Q}+1)} \right] \\ &= \begin{bmatrix} \mathbf{U}_{1,[\bar{Q}]}^{H} \\ \mathbf{u}_{1(\bar{Q}+1)}^{H} \end{bmatrix} \left[\mathbf{U}_{2,[\bar{Q}]}, \mathbf{u}_{2(\bar{Q}+1)} \right] \\ &= \begin{bmatrix} \mathbf{U}_{1,[\bar{Q}]}^{H} \mathbf{U}_{2,[\bar{Q}]} & \mathbf{U}_{1,[\bar{Q}]}^{H} \mathbf{u}_{2(\bar{Q}+1)} \\ \mathbf{u}_{1(\bar{Q}+1)}^{H} \mathbf{U}_{2,[\bar{Q}]} & \mathbf{u}_{1(\bar{Q}+1)}^{H} \mathbf{u}_{2(\bar{Q}+1)} \end{bmatrix} \end{aligned} \tag{B.6}$$

It has been demonstrated in [10] that the first subsample QSS is almost orthogonal to the orthogonal complementary space of the second subsample QSS, that is $\langle \mathbf{U}_{1,[\bar{Q}]} \rangle \perp \langle \bar{\mathbf{U}}_{2,[\bar{Q}]} \rangle$. Likewise, the second subsample QSS is almost orthogonal to the orthogonal complementary space of the first subsample QSS, that is, $\langle \mathbf{U}_{2,[\bar{Q}]} \rangle \perp \langle \bar{\mathbf{U}}_{1,[\bar{Q}]} \rangle$. Since the single noise eigenvectors $\mathbf{u}_{1(\bar{Q}+1)}$ and $\mathbf{u}_{2(\bar{Q}+1)}$ belong to $\langle \bar{\mathbf{U}}_{1,[\bar{Q}]} \rangle$ and $\langle \bar{\mathbf{U}}_{2,[\bar{Q}]} \rangle$, respectively. It can be derived that

$$\begin{cases} \mathbf{u}_{1(\bar{Q}+1)}^{H} \mathbf{U}_{2,[\bar{Q}]} \approx \mathbf{0} \\ \mathbf{U}_{1,[\bar{Q}]}^{H} \mathbf{u}_{2(\bar{Q}+1)} \approx \mathbf{0} \end{cases} \tag{B.7}$$

Therefore, (B.6) can be approximated to

$$\mathbf{U}_{1,[\bar{Q}+1]}^{H} \mathbf{U}_{2,[\bar{Q}+1]} \approx \begin{bmatrix} \mathbf{U}_{1,[\bar{Q}]}^{H} \mathbf{U}_{2,[\bar{Q}]} & \mathbf{0} \\ \mathbf{0} & \mathbf{u}_{1(\bar{Q}+1)}^{H} \mathbf{u}_{2(\bar{Q}+1)} \end{bmatrix} \tag{B.8}$$

Combine (B.4), (B.5) and (B.8), the subspace distance with respect to $l = N - \bar{Q} - 1$ can be transformed to

$$\begin{aligned} d\left(N - \bar{Q} - 1\right) &\approx \bar{Q} + 1 - \left\| \begin{bmatrix} \mathbf{U}_{1,[\bar{Q}]}^{H} \mathbf{U}_{2,[\bar{Q}]} & \mathbf{0} \\ \mathbf{0} & \mathbf{u}_{1(\bar{Q}+1)}^{H} \mathbf{u}_{2(\bar{Q}+1)} \end{bmatrix} \right\|_{F}^{2} \\ &= \bar{Q} - \left\| \mathbf{U}_{1,[\bar{Q}]}^{H} \mathbf{U}_{2,[\bar{Q}]} \right\|_{F}^{2} + 1 - \left\| \mathbf{u}_{1(\bar{Q}+1)}^{H} \mathbf{u}_{2(\bar{Q}+1)} \right\|^{2} \\ &= d\left(\mathbf{U}_{1,[\bar{Q}]}, \mathbf{U}_{2,[\bar{Q}]} \right) + 1 - \left\| \mathbf{u}_{1(\bar{Q}+1)}^{H} \mathbf{u}_{2(\bar{Q}+1)} \right\|^{2} \end{aligned} \tag{B.9}$$

According to the signal subspace proximity, we have

$$d\left(\mathbf{U}_{1,[\bar{Q}]}, \mathbf{U}_{2,[\bar{Q}]} \right) \approx 0 \tag{B.10}$$

Meanwhile, similar to (B.2), the independent property of two noise eigenvectors $\mathbf{u}_{1(\bar{Q}+1)}$ and $\mathbf{u}_{2(\bar{Q}+1)}$ can lead to

$$\left\| \mathbf{u}_{1(\bar{Q}+1)}^{H} \mathbf{u}_{2(\bar{Q}+1)} \right\|^{2} \approx 0 \tag{B.11}$$

As a result, for the point $l = N - \bar{Q} - 1$, the subspace distance also satisfies

$$d\left(N - \bar{Q} - 1\right) \approx 1 \tag{B.12}$$

In addition, as seen from the above derivations, similar to the approximation properties in (20) and (23), the approximation properties described in (B.3) and (B.12) may become more pronounced with a larger sample size.

References

[1] H.L. Van Trees, Optimum Array Processing: Part IV of Detection, Estimation, and Modulation Theory, John Wiley & Sons, 2002.

[2] A. Gershman, E. Nemeth, J. Bohme, Experimental performance of adaptive beamforming in a sonar environment with a towed array and moving interfering sources, IEEE Trans. Signal Process. 48 (2000) 246–250, https://doi.org/10.1109/78.815495.

[3] S. Chen, S. Sun, Q. Gao, X. Su, Adaptive beamforming in tdd-based mobile communication systems: state of the art and 5g research directions, IEEE Wirel. Commun. 23 (2016) 81–87, https://doi.org/10.1109/MWC.2016.1500105WC.
[4] S. Khan, J. Huh, J.C. Ye, Adaptive and compressive beamforming using deep learning for medical ultrasound, IEEE Trans. Ultrason. Ferroelectr. Freq. Control 67 (2020) 1558–1572, https://doi.org/10.1109/TUFFC.2020.2977202.
[5] J. Capon, High-resolution frequency-wavenumber spectrum analysis, Proc. IEEE 57 (1969) 1408–1418, https://doi.org/10.1109/PROC.1969.7278.
[6] B. Carlson, Covariance matrix estimation errors and diagonal loading in adaptive arrays, IEEE Trans. Aerosp. Electron. Syst. 24 (1988) 397–401, https://doi.org/10.1109/7.7181.
[7] Y.-L. Chen, J.-H. Lee, Finite data performance analysis of mvdr antenna array beamformers with diagonal loading, Prog. Electromagn. Res. 134 (2013) 475–507, https://doi.org/10.2528/PIER12092006.
[8] M. Zhang, A. Zhang, Q. Yang, Robust adaptive beamforming based on conjugate gradient algorithms, IEEE Trans. Signal Process. 64 (2016) 6046–6057, https://doi.org/10.1109/TSP.2016.2605075.
[9] O. Besson, An alternative to diagonal loading for implementation of a white noise array gain constrained robust beamformer, Signal Process. 152 (2018) 79–82, https://doi.org/10.1016/j.sigpro.2018.05.019.
[10] X. Chen, W. Sheng, Robust adaptive beamforming via modified variable loading with subsampling preprocessing, Int. J. Antennas Propag. 2022 (2022), https://doi.org/10.1155/2022/2561711.
[11] D. Feldman, L. Griffiths, A projection approach for robust adaptive beamforming, IEEE Trans. Signal Process. 42 (1994) 867–876, https://doi.org/10.1109/78.285650.
[12] F. Huang, W. Sheng, X. Ma, Modified projection approach for robust adaptive array beamforming, Signal Process. 92 (2012) 1758–1763, https://doi.org/10.1016/j.sigpro.2012.01.015.
[13] W. Jia, W. Jin, S. Zhou, M. Yao, Robust adaptive beamforming based on a new steering vector estimation algorithm, Signal Process. 93 (2013) 2539–2542, https://doi.org/10.1016/j.sigpro.2013.03.015.
[14] C. Wang, J. Tang, B. Yang, Fast and convenient implementation of iterative eigenspace-based beamforming, Electron. Lett. 51 (2015) 720–722, https://doi.org/10.1049/el.2015.0131.
[15] J. Li, P. Stoica, Z. Wang, On robust capon beamforming and diagonal loading, IEEE Trans. Signal Process. 51 (2003) 1702–1715, https://doi.org/10.1109/TSP.2003.812831.
[16] S.A. Vorobyov, H. Chen, A.B. Gershman, On the relationship between robust minimum variance beamformers with probabilistic and worst-case distortionless response constraints, IEEE Trans. Signal Process. 56 (2008) 5719–5724, https://doi.org/10.1109/TSP.2008.929866.
[17] Y. Huang, M. Zhou, S.A. Vorobyov, New designs on MVDR robust adaptive beamforming based on optimal steering vector estimation, IEEE Trans. Signal Process. 67 (2019) 3624–3638, https://doi.org/10.1109/TSP.2019.2918997.
[18] Y. Huang, H. Fu, S.A. Vorobyov, Z.-Q. Luo, Robust adaptive beamforming via worst-case SINR maximization with nonconvex uncertainty sets, IEEE Trans. Signal Process. 71 (2023) 218–232, https://doi.org/10.1109/TSP.2023.3240312.
[19] Y. Gu, A. Leshem, Robust adaptive beamforming based on interference covariance matrix reconstruction and steering vector estimation, IEEE Trans. Signal Process. 60 (2012) 3881–3885, https://doi.org/10.1109/TSP.2012.2194289.
[20] X. Yuan, L. Gan, Robust adaptive beamforming via a novel subspace method for interference covariance matrix reconstruction, Signal Process. 130 (2017) 233–242, https://doi.org/10.1016/j.sigpro.2016.07.008.
[21] S. Mohammadzadeh, V.H. Nascimento, R.C. de Lamare, O. Kukrer, Maximum entropy-based interference-plus-noise covariance matrix reconstruction for robust adaptive beamforming, IEEE Signal Process. Lett. 27 (2020) 845–849, https://doi.org/10.1109/LSP.2020.2994527.
[22] X. Zhu, Z. Ye, X. Xu, R. Zheng, Covariance matrix reconstruction via residual noise elimination and interference powers estimation for robust adaptive beamforming, IEEE Access 7 (2019) 53262–53272, https://doi.org/10.1109/ACCESS.2019.2912402.
[23] H. Yang, P. Wang, Z. Ye, Robust adaptive beamforming via covariance matrix reconstruction and interference power estimation, IEEE Commun. Lett. 25 (2021) 3394–3397, https://doi.org/10.1109/LCOMM.2021.3103208.
[24] W. Li, X. Qu, X. Yang, B. Han, Z. Zhang, A.E. Fathy, Robust adaptive beamforming method based on steering vector phase correction and covariance matrix reconstruction, IEEE Commun. Lett. 28 (2024) 193–197, https://doi.org/10.1109/LCOMM.2023.3336217.
[25] S. Mohammadzadeh, V.H. Nascimento, R.C.d. Lamare, O. Kukrer, Covariance matrix reconstruction based on power spectral estimation and uncertainty region for robust adaptive beamforming, IEEE Trans. Aerosp. Electron. Syst. 59 (2023) 3848–3858, https://doi.org/10.1109/TAES.2022.3232100.
[26] L. Huang, J. Zhang, X. Xu, Z. Ye, Robust adaptive beamforming with a novel interference-plus-noise covariance matrix reconstruction method, IEEE Trans. Signal Process. 63 (2015) 1643–1650, https://doi.org/10.1109/TSP.2015.2396002.
[27] Z. Zheng, Y. Zheng, W.-Q. Wang, H. Zhang, Covariance matrix reconstruction with interference steering vector and power estimation for robust adaptive beamforming, IEEE Trans. Veh. Technol. 67 (2018) 8495–8503, https://doi.org/10.1109/TVT.2018.2849646.
[28] X. Zhu, X. Xu, Z. Ye, Robust adaptive beamforming via subspace for interference covariance matrix reconstruction, Signal Process. 167 (2020) 107289, https://doi.org/10.1016/j.sigpro.2019.107289.
[29] S. Sun, Z. Ye, Robust adaptive beamforming based on a method for steering vector estimation and interference covariance matrix reconstruction, Signal Process. 182 (2021) 107939, https://doi.org/10.1016/j.sigpro.2020.107939.
[30] Y. Yang, X. Xu, H. Yang, W. Li, Robust adaptive beamforming via covariance matrix reconstruction with diagonal loading on interference sources covariance matrix, Digit. Signal Process. 136 (2023) 103977, https://doi.org/10.1016/j.dsp.2023.103977.
[31] H. Ruan, R.C. de Lamare, Robust adaptive beamforming using a low-complexity shrinkage-based mismatch estimation algorithm, IEEE Signal Process. Lett. 21 (2014) 60–64, https://doi.org/10.1109/LSP.2013.2290948.
[32] Z. Zhang, W. Liu, W. Leng, A. Wang, H. Shi, Interference-plus-noise covariance matrix reconstruction via spatial power spectrum sampling for robust adaptive beamforming, IEEE Signal Process. Lett. 23 (2016) 121–125, https://doi.org/10.1109/LSP.2015.2504954.
[33] S. Mohammadzadeh, V.H. Nascimento, R.C. De Lamare, O. Kukrer, Robust adaptive beamforming based on low-complexity discrete Fourier transform spatial sampling, IEEE Access 9 (2021) 84845–84856, https://doi.org/10.1109/ACCESS.2021.3088747.
[34] T. Luo, P. Chen, Z. Cao, L. Zheng, Z. Wang, URGLQ: an efficient covariance matrix reconstruction method for robust adaptive beamforming, IEEE Trans. Aerosp. Electron. Syst. 59 (2023) 5634–5645, https://doi.org/10.1109/TAES.2023.3263386.
[35] S. Mohammadzadeh, O. Kukrer, Robust adaptive beamforming based on covariance matrix and new steering vector estimation, Signal Image Video Process. 13 (2019) 853–860, https://doi.org/10.1007/s11760-019-01421-8.
[36] H. Yang, Z. Ye, Robust adaptive beamforming based on covariance matrix reconstruction via steering vector estimation, IEEE Sens. J. 23 (2023) 2932–2939, https://doi.org/10.1109/JSEN.2022.3228854.
[37] S. Mohammadzadeh, V.H. Nascimento, R.C. de Lamare, O. Kukrer, Jammer tracking based on efficient covariance matrix reconstruction with iterative spatial spectrum sampling, IEEE Trans. Aerosp. Electron. Syst. 59 (2023) 8681–8695, https://doi.org/10.1109/TAES.2023.3307507.
[38] A. Edelman, T.A. Arias, S.T. Smith, The geometry of algorithms with orthogonality constraints, SIAM J. Matrix Anal. Appl. 20 (1998) 303–353, https://doi.org/10.1137/S0895479895290954.
[39] L. Wang, X. Wang, J. Feng, Subspace distance analysis with application to adaptive Bayesian algorithm for face recognition, Pattern Recognit. 39 (2006) 456–464, https://doi.org/10.1016/j.patcog.2005.08.015.
[40] Z. Huang, R. Wang, S. Shan, X. Chen, Projection metric learning on Grassmann manifold with application to video based face recognition, in: 2015 IEEE Conference on Computer Vision and Pattern Recognition (CVPR), Boston, MA, JUN 07-12, 2015, in: IEEE Conference on Computer Vision and Pattern, IEEE, 2015, pp. 140–149.
[41] X. Mestre, On the asymptotic behavior of the sample estimates of eigenvalues and eigenvectors of covariance matrices, IEEE Trans. Signal Process. 56 (2008) 5353–5368, https://doi.org/10.1109/TSP.2008.929662.
[42] H. Subbaram, K. Abend, Interference suppression via orthogonal projections: a performance analysis, IEEE Trans. Antennas Propag. 41 (1993) 1187–1194, https://doi.org/10.1109/8.247744.
[43] J. Zhuang, A. Manikas, Interference cancellation beamforming robust to pointing errors, IET Signal Process. 7 (2013) 120–127, https://doi.org/10.1049/iet-spr.2011.0464.
[44] J. Yang, G. Liao, J. Li, Y. Lei, X. Wang, Robust beamforming with imprecise array geometry using steering vector estimation and interference covariance matrix reconstruction, Multidimens. Syst. Signal Process. 28 (2017) 451–469, https://doi.org/10.1007/s11045-015-0350-7.

Xiangwei Chen was born in 1992, he is currently pursuing the Ph.D. degree from Nanjing University of Science and Technology. His research interests lie in the areas of array signal processing and statistical signal processing.

Weixing Sheng was born in 1966, he is currently a professor with the School of Electronic and Optical Engineering, Nanjing University of Science and Technology. His research interests lie in the areas of radar signal processing, array signal processing, modeling and application of electromagnetic scattering, and image processing.